



Glassy and liquid Sb₂S₃: insight into the structure and dynamics of a promising functional material

Mohammad Kassem, Chris Benmore, Andrey Tverjanovich, Takeshi Usuki, Maxim Khomenko, Daniele Fontanari, Anton Sokolov, Koji Ohara, Maria Bokova, Shinji Kohara, et al.

► To cite this version:

Mohammad Kassem, Chris Benmore, Andrey Tverjanovich, Takeshi Usuki, Maxim Khomenko, et al.. Glassy and liquid Sb₂S₃: insight into the structure and dynamics of a promising functional material. Journal of Materials Chemistry C, 2023, 11 (14), pp.4654-4673. 10.1039/D3TC00081H . hal-04124971

HAL Id: hal-04124971

<https://hal.science/hal-04124971>

Submitted on 11 Jun 2023

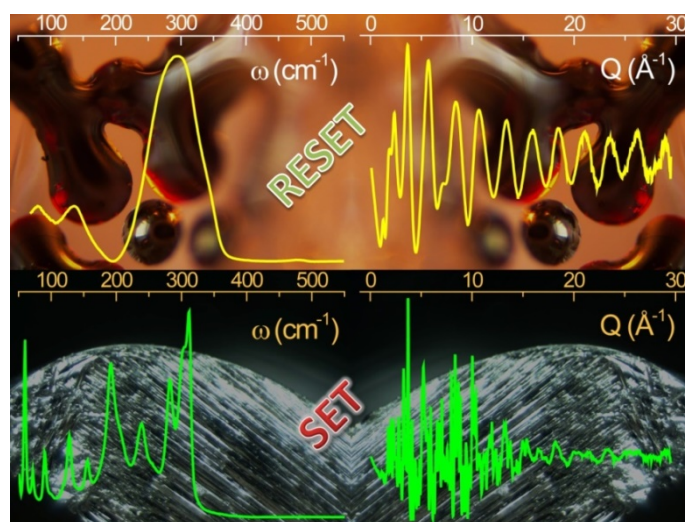
HAL is a multi-disciplinary open access archive for the deposit and dissemination of scientific research documents, whether they are published or not. The documents may come from teaching and research institutions in France or abroad, or from public or private research centers.

L'archive ouverte pluridisciplinaire **HAL**, est destinée au dépôt et à la diffusion de documents scientifiques de niveau recherche, publiés ou non, émanant des établissements d'enseignement et de recherche français ou étrangers, des laboratoires publics ou privés.

Glassy and Liquid Sb_2S_3 : Insight into the Structure and Dynamics of Promising Functional Material

Mohammad Kassem, Chris J. Benmore, Andrey Tverjanovich, Takeshi Usuki, Maxim Khomenko, Daniele Fontanari, Anton Sokolov, Koji Ohara, Maria Bokova, Shinji Kohara, and Eugene Bychkov*

ABSTRACT: Antimony sesquisulfide Sb_2S_3 has become an outstanding advanced functional material in a variety of rapidly growing application fields: smart integrated photonics from the visible to telecom window, cost-efficient photovoltaics, energy storage and transformation. Rational design and tailoring of the required components needs a deep insight into the atomic structure and dynamics of liquid and amorphous Sb_2S_3 , but the detailed information is missing in contrast to crystalline counterparts. Using high-energy X-ray diffraction and Raman spectroscopy over an extended temperature range, supported by first-principles simulations as well as by electrical and thermal studies, we show that the high optical and electric contrast between the SET (crystalline) and RESET (amorphous) logic states is related to the different short and intermediate range order in orthorhombic and vitreous Sb_2S_3 . It includes a strong asymmetry of the Sb-S nearest neighbor distances and a different coordination of antimony sites in the crystal vs. a distorted trigonal environment of defect octahedral SbS_3 entities in glassy Sb_2S_3 . Fast crystallization rate at elevated temperatures in liquid antimony sesquisulfide is related to the enhanced fragility, approaching that of telluride phase-change materials, and to a large fraction of *ABAB* squares (*A*: Sb; *B*: S), combined with a remarkable slowdown of the diffusion processes in the vicinity of the glass transition temperature, ensuring a good retention of the amorphous state. Further improvements maybe achieved using anionic (Se) or cationic (Bi) substitution that decreases the temperature of a semiconductor-metal transition and allows bandgap engineering, important for both photonics and photovoltaics.



TOC Figure

* email address: bychkov@univ-littoral.fr

1. INTRODUCTION

Antimony sesquisulfide Sb_2S_3 appears to be emerging and promising advanced functional material for a variety of rapidly growing application fields:

(1) *Wide gap phase-change material (PCM) for both electrically and light tunable visible photonics or ultralow loss photonics at telecommunication wavelengths.* Sb_2S_3 can be used for smart reprogrammable photonic systems with a nanosecond switching time, holographic and nonvolatile ultrathin displays of extremely high resolution, integrated photonic circuits, switchable metasurfaces and varifocal metalens, nanophotonic and on-chip devices, dielectric nanoantennas, etc.¹⁻⁶

(2) *High-performance composite anode for sodium and lithium batteries.* Antimony sesquisulfide nanorods, nanoparticles and powders, sometimes combined with other sulfides and encapsulated into doped carbon matrix or activated carbon, provide a superior rate capability, excellent cyclic stability and capacity retention, as well as fast-charging capacity and highly decreased interfacial resistance.⁷⁻¹⁰

(3) *Alternative absorber material for thin-film solar cells.* Antimony sulfide thin films belong to emerging earth-abundant low-cost photovoltaic materials having reasonable optical bandgap, tremendous low-light harvesting, excellent moisture and air stability.^{11,12}

(4) *Thermoelectric material.* High thermoelectric power of Sb_2S_3 seems to be promising for thermoelectric applications.¹³ However, nanostructured or amorphous antimony sesquisulfide is mostly used as a dopant decreasing the thermal conductivity and increasing the Seebeck coefficient of composite thermoelectrics (lead chalcogenides, $(\text{Bi,Sb})_2\text{Te}_3$, etc.) yielding a significantly enhanced figure of merit zT .^{14,15}

Rational design and tailoring of optimized functional materials based on Sb_2S_3 need a deep insight into the atomic structure and dynamics of antimony sesquisulfide. The crystal structure of Sb_2S_3 has been extensively studied both at ambient conditions¹⁶⁻¹⁸ and under high pressure.¹⁹⁻²⁶ Nevertheless, the atomic structure of vitreous and liquid antimony sesquisulfide is largely unknown except for classical X-ray diffraction studies of glassy Sb_2S_3 reported forty years ago and suffering from a limited accessible Q -range and insufficient r -space resolution.²⁷⁻²⁹ In case of PCM applications,³⁰⁻³² a special attention should be paid to the origin of a high optical and electric contrast between the SET (crystalline) and RESET (amorphous) logic states since antimony sesquisulfide differs considerably from the benchmark telluride PCM ($\text{GeTe-Sb}_2\text{Te}_3$, GST, or doped Sb_2Te_3) in both chemical bonding and local antimony environment. The metavalent bonding³³ seems to be missing in Sb_2S_3 ; and the four-fold coordinated antimony sites, present in GST and $\alpha\text{-Sb}_2\text{Te}_3$,^{34,35} were not observed in vitreous Sb_2S_3 ,²⁷⁻²⁹ even though there is a controversy in amorphous tellurides related to the antimony local order.^{36,37}

Using high-energy X-ray diffraction and Raman spectroscopy supported by first-principles simulations, we will unravel a detailed structural organization of bulk glassy and liquid Sb_2S_3 over an extended temperature range, $298 \leq T \leq 1143$ K. Thermal properties and electrical conductivity measurements will also be provided showing a remarkable contrast in electronic properties between amorphous, crystalline and liquid states. Finally, diffusion coefficients and viscosity of liquid Sb_2S_3 will be computed and compared with known experimental data, which reveal a significant fragility of molten antimony sesquisulfide in comparison with canonical dielectric As_2S_3 . All these results will explain promising PCM performance of Sb_2S_3 and an overall trend in functional properties going down on the Periodic Table.

2. EXPERIMENTAL SECTION

2.1. Glassy Sb_2S_3 Preparation. A two-step synthesis was applied for glassy Sb_2S_3 . First, a crystalline sample was prepared from high-purity antimony (99.999%, Cerac) and sulfur (99.999%, Alfa Aesar) in evacuated and sealed silica tube. Then, a small quantity of $c\text{-Sb}_2\text{S}_3$ was placed in a thin-walled silica capillary, evacuated to 10^{-4} mbar and sealed. The capillary was slowly heated in a furnace to 1050 K and kept at this temperature for one hour with subsequent cooling to 900 K. After additional equilibration step for at least 30 minutes, the sample was splat-quenched under argon atmosphere onto a fused silica plate cooled down to ≈ 250 K.

2.2. Thermal and Electrical Measurements. A TA instruments Q200 thermal analyzer was used for differential scanning calorimetry (DSC). The synthesized samples of 3-5 mg were encapsulated in a sealed aluminum pan and heated at a rate of 10 K min^{-1} under a dry nitrogen atmosphere to determine the glass transition T_g and crystallization temperatures. The ac and dc conductivity measurements were done over the $330 \leq T \leq 450 \text{ K}$ temperature range. A Hewlett Packard 4339B high resistance meter with applied voltage of 100 volts was used for the dc experiments. The ac conductivity over the 100 Hz to 15 MHz frequency range was measured using a Hewlett Packard 4194A impedance meter.

2.3. Raman Spectroscopy Measurements. A LabRam HR microRaman spectrometer (Jobin Yvon Horiba Group) was used for the measurements at room temperature. Raman scattering was excited by a 785 nm solid-state laser and recorded in the $50\text{--}850 \text{ cm}^{-1}$ spectral range. The laser power was 0.75 mW. Two to three spectra were registered for each sample at different positions to verify the sample homogeneity and the absence of photoinduced phenomena. Raman spectra over the temperature range $293 \leq T \leq 873 \text{ K}$ were measured using a Senterra Raman spectrometer (Bruker) equipped with a microscope and a Linkam TS1000 hot stage. The spectra were excited by a 785 nm laser diode with a power of 1 mW and recorded in the $75\text{--}1500 \text{ cm}^{-1}$ spectral range (reliable data above 100 cm^{-1}). Glassy Sb_2S_3 was placed in a silica tube (2 mm ID/3 mm OD, length 12 mm) and sealed under vacuum.

2.4. High-Energy X-ray Diffraction. The 6-ID-D beamline at the Advanced Photon Source (Argonne National Laboratory, Chicago) was used for high-energy X-ray diffraction measurements at ambient conditions and as a function of temperature. The photon energy was 99.9593 keV, and the wavelength was 0.124035 \AA . A two-dimensional (2D) setup was used for data collection with a Varex area detector, 2880×2880 pixels, and a pixel size of $150 \times 150 \mu\text{m}^2$. The sample-to-detector distance was 287.7 mm for a room-temperature setup, and 334.9 mm for furnace measurements over the $673 \leq T \leq 1143 \text{ K}$ temperature range on cooling. Cerium dioxide was used as a calibrant. The exposure time was $0.2 \text{ s} \times 1500$ frames, using one dark-field image file followed by five light files. Glass samples were fixed on a Kapton tape for the room temperature measurements. A Sb_2S_3 sample in evacuated silica tube (2 mm ID/3 mm OD) was used for the furnace experiments. The 2D diffraction patterns were reduced using the Fit2D software.³⁸ The measured background intensity (either the Kapton tape or the empty silica at

various temperatures) was subtracted, and corrections were made for the different detector geometries and efficiencies, sample self-attenuation, and Compton scattering using standard procedures,³⁹ providing the X-ray structure factor $S_X(Q)$.

$$S_X(Q) = w_{\text{SbSb}}(Q)S_{\text{SbSb}}(Q) + w_{\text{SbS}}(Q)S_{\text{SbS}}(Q) + w_{\text{SS}}(Q)S_{\text{SS}}(Q), \quad (1)$$

where $w_{ij}(Q)$ are Q -dependent X-ray weighting coefficients and $S_{ij}(Q)$ the Faber-Ziman partial structure factors.

Canonical As_2S_3 glass and liquid were also measured at the BL04B2 beamline of the SPring-8 facility (Hyogo Prefecture, Japan) using a dedicated two-axis diffractometer equipped with four CdTe detectors at low angles and three Ge diodes at high diffraction angles.⁴⁰ The temperature measurements were carried out from 300 to 1223 K in a furnace. The 7-detector setup and incident X-ray energy of 112.6386 keV allows the diffraction pattern to be collected up to $Q = 30 \text{ \AA}^{-1}$ with a high signal-to-noise ratio and sufficient energy resolution to discriminate both fluorescence from the sample and higher harmonic reflections from the monochromator crystal. The empty silica tube at different temperatures was also measured and used for background intensity subtraction. Further data analysis included absorption, Compton scattering, and polarization corrections using standard procedures⁴¹ giving the total X-ray structure factor $S_X(Q)$.^{42,43}

2.5. First-Principles Simulations. The DFT calculations of vibrational spectra were carried out using Gaussian 16 software.⁴⁴ The structural optimization and harmonic vibrational frequency calculations were performed for size-limited clusters: SbSb_3H_3 , SbS_3H_3 , $\text{Sb}_2\text{S}_4\text{H}_2$ (chair and boat conformations), $\text{Sb}_2\text{S}_5\text{H}_4$, $\text{Sb}_2\text{S}_6\text{H}_4$, $\text{Sb}_3\text{S}_6\text{H}_3$, $\text{Sb}_6\text{S}_{12}\text{H}_6$, $\text{Sb}_{12}\text{S}_{18}\text{H}_2$, and $\text{Sb}_{12}\text{S}_{16}$. The Becke three-parameter hybrid exchange functional⁴⁵ and the Lee–Yang–Parr correlation functional (B3LYP)⁴⁶ were used for these simulations. The small-core relativistic pseudopotential basis set (cc-pVTZ-PP)⁴⁷ and the effective core potentials⁴⁸ were applied for cluster geometry optimization and Raman intensity calculations. Most of the structures were optimized using the tight convergence option ensuring adequate convergence and reliability of computed wavenumbers. Extra quadratically convergent self-consistent field procedure⁴⁹ was used for difficult convergence cases. Further details of the DFT simulations are reported elsewhere.^{50–52}

Modeling of the diffraction data was carried out using Born–Oppenheimer molecular dynamics implemented within the CP2K package.⁵³ The generalized gradient approximation (GGA) and the PBE0 hybrid^{54,55} exchange–correlation functional combining the exact Hartree–Fock and DFT approaches were used, providing a better agreement with experiment.^{56–59} The Grimme dispersion corrections D3BJ⁶⁰ were also employed, improving first-principles molecular dynamics (FPMD) results for chalcogenide systems.^{61,62} The applied FPMD technique was similar to previous reports.^{34,63} The initial atomic configurations for vitreous Sb_2S_3 were created and optimized using the RMC_POT++ code⁶⁴ against the experimental $S_X(Q)$. The size of the cubic simulation box, containing 200 atoms (80 Sb and 120 S), was chosen to match the experimental density. Further optimization was carried out using DFT, applying the molecularly optimized correlation consistent polarized triple-zeta valence basis set along with the norm-conserving relativistic Goedecker–Teter–Hutter-type pseudopotentials.⁶⁵ FPMD simulations were performed using a canonical NVT ensemble with a Nosé–Hoover^{66,67} thermostat. The simulation boxes were heated from 300 K to 900 K using 100 K steps for 20–25 ps each. At 900

K (above melting), the systems were equilibrated for 70 ps and cooled down to 300 K using the same temperature steps but with a longer simulation time (25-45 ps). Final equilibration and data collection at 300 K were performed for 59 ps. Additional simulations were carried out between 850 and 1150 K (step 100 K for 40-50 ps each) consistent with experimental data. The connectivity and ring statistics were analyzed using the R. I. N. G. S. package⁶⁸ and a modified connectivity program.⁶⁹ The pyMolDyn code⁷⁰ applying the Dirichlet–Voronoi tessellation was used for the calculation of microscopic voids and cavities.

3. RESULTS AND DISCUSSION

3.1. Glass-Forming, Thermal and Electric Properties. Glassy antimony sesquisulfide was reported to be a difficult material to vitrify.²⁷ Nevertheless, the applied splat-quenching technique⁵⁶ in thin-walled silica capillaries allows fully vitreous small droplets of *g*-Sb₂S₃ to be obtained. Typical DSC traces for glassy Sb₂S₃ and canonical *g*-As₂S₃ are shown in Figure 1. The two end-members are consistent with the reported thermal properties for (Sb₂S₃)_x(As₂S₃)_{1-x} pseudo-binaries, $x \leq 0.9$:⁷¹⁻⁷³ the glass transition temperature T_g monotonically increases with x from 472 K ($x = 0$) to 492 K ($x = 1$), the exothermic crystallization feature emerges above $x = 0.5$, grows and shifts toward lower T , emphasizing the increasing crystallization ability.

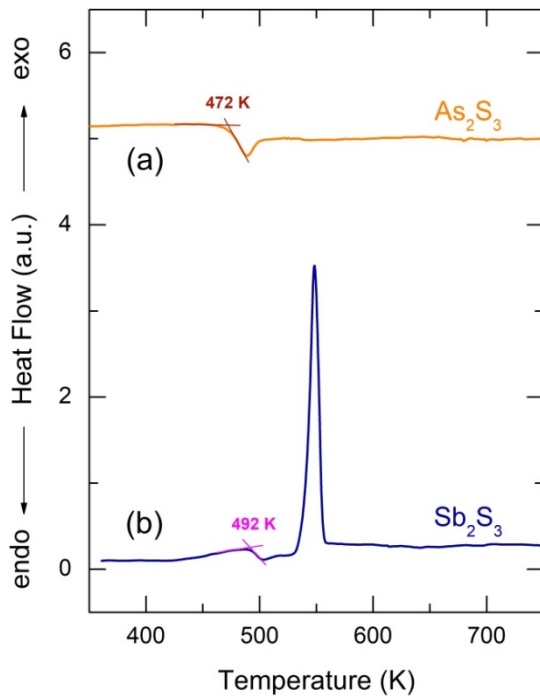


Figure 1. DSC traces of glassy (a) As₂S₃ and (b) Sb₂S₃. The derived glass transition temperatures are also indicated.

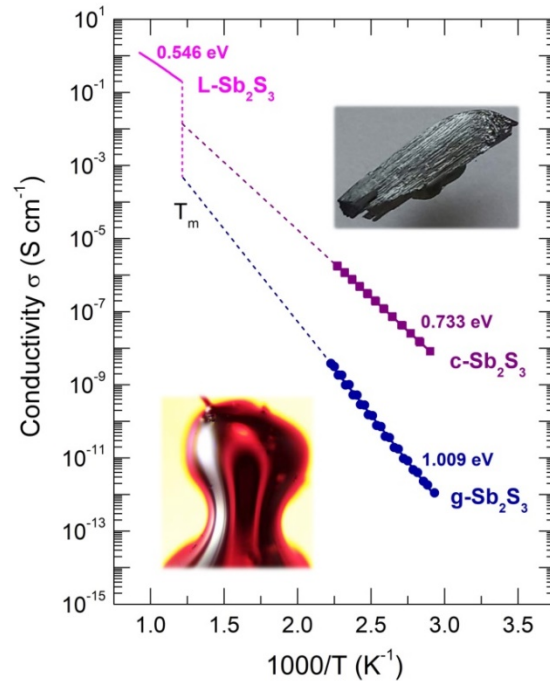


Figure 2. Conductivity $\sigma(T)$ of glassy (*g*), crystalline (*c*) samples (this work), and liquid *L*-Sb₂S₃.⁷⁴ The inserts show *g*-Sb₂S₃ and *c*-Sb₂S₃.

The conductivity temperature dependences $\sigma(T)$ for glassy and crystalline (this work), and molten⁷⁴ Sb₂S₃ are shown in Figure 2 using an Arrhenius plot:

$$\sigma(T) = \sigma_0 \exp(-E_a/k_B T), \quad (2)$$

where σ_0 is the pre-exponential factor, E_a the conductivity activation energy, and k_B and T have their usual meaning. We note a significant electrical contrast between glassy and crystalline

samples, ≈ 4.5 orders of magnitude at room temperature with corresponding difference in activation energy, $E_a^{\text{cryst}} = 0.733$ eV but $E_a^{\text{glass}} = 1.009$ eV. The conductivity increases on melting by three orders of magnitude compared to extrapolated glass value, while the activation energy drops nearly by a factor of 2. The pre-exponential factor appears to be very similar for all three Sb_2S_3 phases, $400 \leq \sigma_0 \leq 800$ S cm $^{-1}$, and indicates a conductivity mechanism over extended (delocalized) electron states.⁷⁵ The obtained results are consistent with the reported values of conductivity parameters and optical bandgap E_g for bulk crystalline samples and amorphous or crystalline thin films, $1.5 \leq E_g(c\text{-Sb}_2\text{S}_3) \leq 1.8$ eV and $2.0 \leq E_g(a\text{-Sb}_2\text{S}_3) \leq 2.4$ eV.^{1,76-79} In addition, the conductivity seems to be intrinsic since $2E_a \cong E_g$.

3.2. Nanocrystalline Sb_2S_3 . Insufficiently rapid quenching rate or wrong starting temperature for splat-cooling yields a nanocrystalline alloy, which is slightly different from the stable orthorhombic polymorph, space group $Pnma$.¹⁶ The observed Bragg peaks mostly correspond to orthorhombic antimony sesquisulfide, but we should note slight deviations of the peak positions and their different amplitudes compared to the reference compound, Figure 3a. Besides, a non-negligible amorphous fraction is also present and possibly some traces of monoclinic high- T Sb_2S_3 polymorph, which is metastable at room temperature.¹⁸

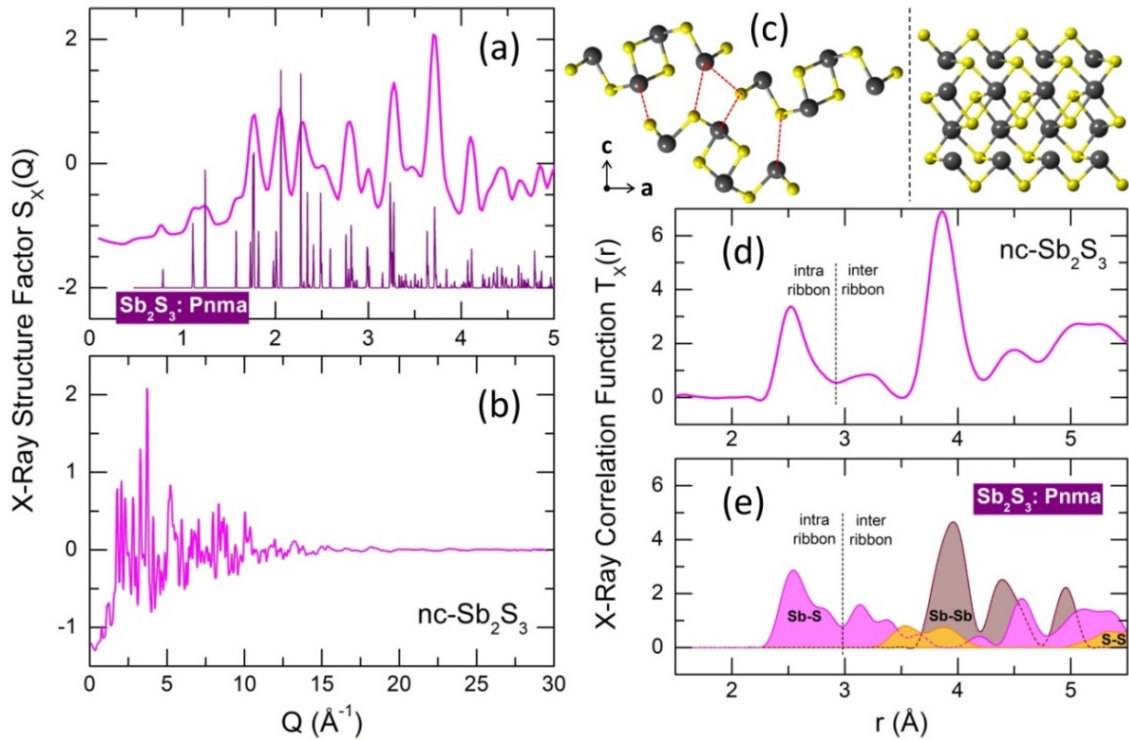


Figure 3. Nanocrystalline (nc) and orthorhombic Sb_2S_3 . (a) Bragg peaks of the nanocrystalline sample in comparison with orthorhombic polymorph¹⁶ space group $Pnma$; (b) X-ray structure factor $S_x(Q)$ over the entire Q -range; (c) $(\text{Sb}_4\text{S}_6)_\infty$ ribbons in orthorhombic Sb_2S_3 : *left*, atomic arrangements using projection on the (a, c) plane, *right*, a single ribbon oriented parallel to the b axis; (d) X-ray total correlation function $T_x(r)$ of $nc\text{-Sb}_2\text{S}_3$; (e) Sb-S (magenta), Sb-Sb (light brown) and S-S (yellow) $T_{ij}(r)$ partials for orthorhombic Sb_2S_3 . The dashed red lines in (c), *left* panel, show the shortest inter-ribbon Sb-S distances (3.167-3.642 \AA). The black dashed lines in (d) and (e) separate intra- (2.455-2.854 \AA) and inter-ribbon Sb-S nearest contacts.

The X-ray total correlation function $T_X(r)$ of nanocrystalline Sb_2S_3 , Figure 3d, obtained by the usual Fourier transform of the structure factor $S_X(Q)$, Figure 3b,

$$T_X(r) = 4\pi\rho_0 r + \frac{2}{\pi} \int_0^{Q_{\max}} Q[S_X(Q) - 1] \sin Qr M(Q) dQ, \quad (3)$$

where $M(Q)$ is a modification function and ρ_0 is the experimental number density, confirms characteristic differences between nanocrystalline and orthorhombic antimony sesquisulfides. The latter is formed by infinite quasi one-dimensional (1D) $(\text{Sb}_4\text{S}_6)_\infty$ ribbons oriented parallel to the **b** axis, Figure 3c. The inner Sb(II) atoms have 5 sulfur neighbors forming a distorted square pyramid with Sb(II) species located 0.17 Å below the basal plan of the pyramid. The outer Sb(I) counterparts reside at the apex of trigonal SbS_3 units connected by two-fold sulfur at the ribbon periphery and three-fold sulfur toward Sb(II) and the ribbon interior. The average intra-ribbon antimony coordination appears to be $\langle N_{\text{Sb-S}}^{\text{intra}} \rangle = 4$ while their sulfur neighbors have $\langle N_{\text{S-Sb}}^{\text{intra}} \rangle = 2.67$. The Sb(II)-S nearest neighbor (NN) distances reveal a strong Peierls distortion, $r_{\text{Sb(II)-S}}^{5\text{F}} = 2.70 \pm 0.16$ Å, while the intra-ribbon contacts for trigonal Sb(I) are uniform, $r_{\text{Sb(I)-S}}^{3\text{F}} = 2.53 \pm 0.01$ Å. The 1D- $(\text{Sb}_4\text{S}_6)_\infty$ entities are held together by rather strong inter-ribbon forces forming puckered sheets within the (**a**, **c**) plane. The shortest Sb-S inter-ribbon distances, $3.167 \leq r_{\text{Sb-S}}^{\text{inter}} \leq 3.642$ Å, are smaller than the sum of the van der Waals radii, $r_{\text{S}}^{\text{vdW}} = 1.8$ Å and $r_{\text{Sb}}^{\text{vdW}} = 2.2$ Å,⁸⁰ but larger than the Sb-S intra-ribbon NN contacts, $2.455 \leq r_{\text{Sb-S}}^{\text{intra}} \leq 2.854$ Å. The intra- and inter-ribbon separations are well distinguished using the $T_{\text{SbS}}(r)$ partials for both orthorhombic and nanocrystalline Sb_2S_3 , Figure 3d,e. The main difference between the two forms resides in the inter-ribbon connectivity. In average, each antimony in orthorhombic Sb_2S_3 has three short Sb-S inter-ribbon contacts, $\langle N_{\text{Sb-S}}^{\text{inter}} \rangle = 3$, while the connectivity in *nc*- Sb_2S_3 is reduced, $\langle N_{\text{Sb-S}}^{\text{inter}} \rangle \approx 1.5$. In other words, the 1D- $(\text{Sb}_4\text{S}_6)_\infty$ ribbons are becoming more isolated in nanocrystalline lattice.

3.3. Raman Spectroscopy and DFT Modeling. Typical Raman spectra of glassy Sb_2S_3 as a function of temperature are shown in Figure 4b. The temperatures between $293 \leq T \leq 423$ K correspond to the solid glass, Figure 4a. Above $T_g = 492$ K, the supercooled liquid rapidly crystallizes at 523 K, Figure 4c, just in the vicinity of DSC crystallization onset. Cooling down the crystallized sample, one obtains a typical spectrum of orthorhombic Sb_2S_3 , characterized by multiple Raman-active modes $\Gamma = 10A_g + 5B_{1g} + 10B_{2g} + 5B_{3g}$, expected for the *Pnma* polymorph.⁸¹ Usually, about ten modes are clearly distinguishable.^{20,21,26}

The Raman spectrum of *L*- Sb_2S_3 at 873 K appears to be reminiscent of its glassy counterpart, Figure 4d, except for a strong S-S stretching at 490 cm^{-1} . Assuming a dissociation reaction $2\text{Sb-S} \rightleftharpoons \text{Sb-Sb} + \text{S-S}$, we also should expect a broad Sb-Sb stretching at ≈ 145 cm^{-1} as in amorphous antimony,^{82,83} also confirmed by DFT modeling, Figure S1 in the Supporting Information. A low-frequency vibration feature below 180 cm^{-1} may contain both Sb-S bending and Sb-Sb stretching. We should however note that the appearance of intense S-S stretching in liquid Sb_2S_3 can be a transient phenomenon. Previously, both sulfur and antimony were detected on heating or laser-induced processing of amorphous Sb_2S_3 thin films, partly as intermediate species.⁸⁴⁻⁸⁷ A limited accessible temperature range for our in situ Raman measurements does not enable further experiments at higher *T*. Nevertheless, a temperature-dependent dynamics on melting was observed over a limited *T*-range, Figure S2.

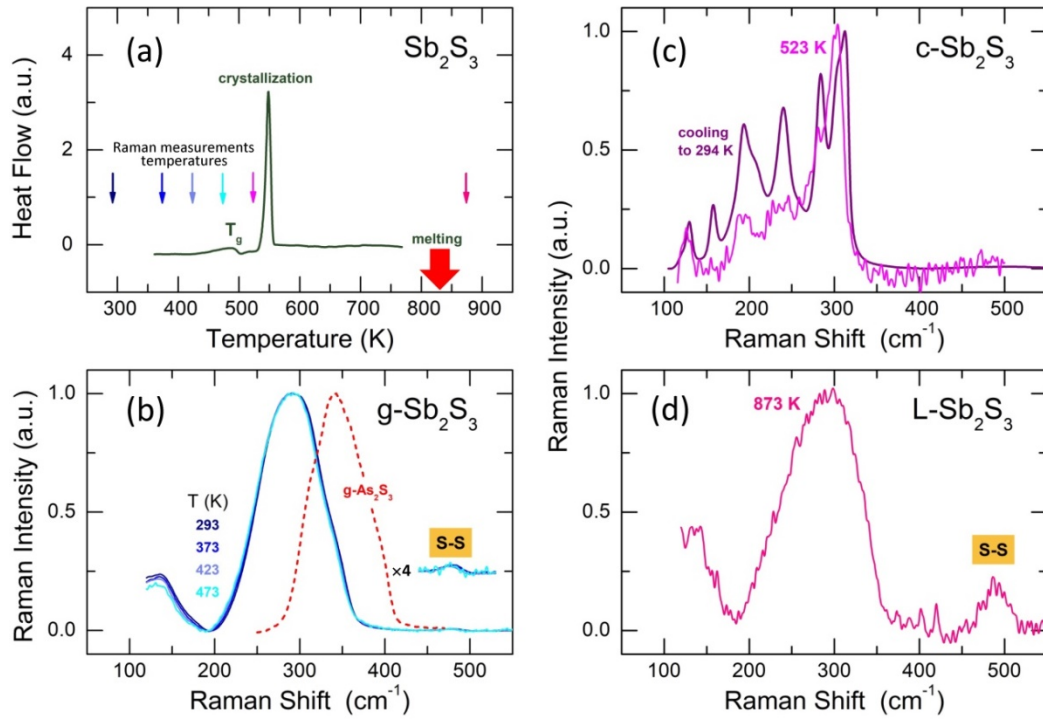


Figure 4. Raman spectra of antimony sesquisulfide: (a) DSC trace of $g\text{-Sb}_2\text{S}_3$, the arrows show the Raman measurement temperatures; (b) spectra of a solid glass as a function of temperature, the insert shows S-S stretching at $\approx 490\text{ cm}^{-1}$; (c) spectra of orthorhombic polymorph at 523 K and after cooling to room temperature; (d) Raman spectrum of molten Sb_2S_3 at 873 K. The dashed red line in (b) also shows the As-S stretching envelope in $g\text{-As}_2\text{S}_3$. See text for further details.

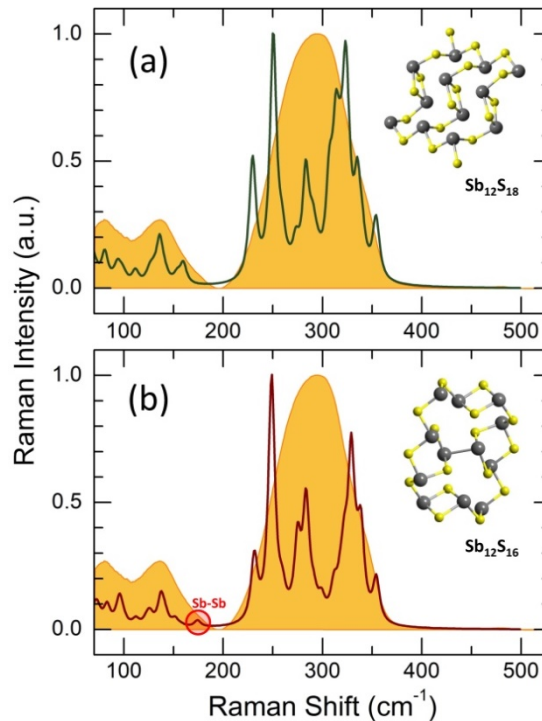


Figure 5. DFT Raman spectra of (a) $\text{Sb}_{12}\text{S}_{18}\text{H}_2$ and (b) $\text{Sb}_{12}\text{S}_{16}$ size-limited clusters in comparison with experimental Raman spectrum of $g\text{-Sb}_2\text{S}_3$, highlighted in yellow for the two panels. The terminal hydrogen species in (a) are omitted, and the H-related vibrations are removed from the spectrum. The inserts show DFT-optimized clusters. Weak Sb-Sb stretching in (b) is emphasized by the red circle.

Basically, a broad asymmetric unresolved feature centered at $\nu_{\max}^{\text{Sb}_2\text{S}_3} \approx 292 \text{ cm}^{-1}$ in glassy Sb_2S_3 is similar to that in $g\text{-As}_2\text{S}_3$ ($\nu_{\max}^{\text{As}_2\text{S}_3} \approx 340 \text{ cm}^{-1}$) but shifted to lower frequencies, Figure 4b, roughly scaling with the molecular mass ratio, $\nu_{\max}^{\text{Sb}_2\text{S}_3} / \nu_{\max}^{\text{As}_2\text{S}_3} \approx \sqrt{M_{\text{As}_2\text{S}_3} / M_{\text{Sb}_2\text{S}_3}}$. Amorphous $\alpha\text{-Sb}_2\text{S}_3$ thin films and antimony-containing bulk sulfide glasses reveal similar vibrational features.^{2,88-92} Assuming trigonal antimony local coordination²⁷ and the above resemblance in Raman spectra, various DFT simulations have been carried out. Isolated pyramidal units SbS_3H_3 , corner- $\text{CSb}_2\text{S}_5\text{H}_4$ and edge-sharing $\text{ESb}_2\text{S}_4\text{H}_2$ dimers of different conformation, and small rings, $\text{Sb}_3\text{S}_6\text{H}_3$ or $\text{Sb}_6\text{S}_{12}\text{H}_6$, systematically reveal overestimated Sb-S stretching frequencies, centered at $320 \leq \langle \nu_{\max}^{\text{Sb-S}} \rangle \leq 350 \text{ cm}^{-1}$, Figure S3 in the Supporting Information. Reasonable results yield complicated clusters $\text{Sb}_{12}\text{S}_{18}\text{H}_2$ and $\text{Sb}_{12}\text{S}_{16}$, originating from the modified ribbons in orthorhombic Sb_2S_3 but with exclusively trigonal antimony coordination, Figure 5. Both symmetric and asymmetric stretching frequencies, as well as low-frequency bending and deformation modes below 190 cm^{-1} are well reproduced by these clusters. As expected, the Sb-Sb stretching in $\text{Sb}_{12}\text{S}_{16}$ is overlapping with Sb-S bending and deformation making impossible to distinguish these vibrations experimentally. In contrast, the S-S stretching at 490 cm^{-1} is clearly visible in Raman scattering, Figure 4b,d, and confirmed by DFT simulations, Figure S3, cluster $\text{Sb}_2\text{S}_6\text{H}_4$. The geometry of DFT-optimized size-limited clusters is consistent with crystalline references and glassy Sb_2S_3 , Figure S4 and S5, specifically that of $\text{Sb}_{12}\text{S}_{18}\text{H}_2$ and $\text{Sb}_{12}\text{S}_{16}$.

Raman spectroscopy measurements show that the glass structure hardly evolves at $T \lesssim T_g$; a negligible red shift of the Sb-S stretching envelope can only be observed, Figure 4b. The rapid crystallization above T_g seems to be related to the presence of modified structural motifs originating from the $(\text{Sb}_4\text{S}_6)_\infty$ entities, although the Sb(II) species lose their 5-fold coordination in the glass. Further insight into the atomic glass structure yields high-energy X-ray diffraction supported by first-principles molecular dynamics (FPMD).

3.4. High-Energy X-Ray Diffraction over the Extended Temperature Range. Typical X-ray structure factors $S_X(Q)$ for $g\text{-Sb}_2\text{S}_3$, supercooled (673–773 K) and normal ($T \geq 843 \text{ K}$) liquids are shown in Figure 6a-c. The $S_X(Q)$'s exhibit well-defined oscillations up to 30 \AA^{-1} , ensuring high-resolution in the r -space. The oscillations amplitude decreases with increasing temperature but more significant changes are observed at low $Q \lesssim 5 \text{ \AA}^{-1}$.

Except distinct first sharp diffraction peak (FSDP) at $Q_0 = 1.22 \text{ \AA}^{-1}$, typical for a large majority of chalcogenide glasses, glassy Sb_2S_3 reveals an additional low- Q feature at $Q_{\text{Sb}} = 1.75 \text{ \AA}^{-1}$, specific for antimony, which emerges and increases in glassy $(\text{Sb}_2\text{S}_3)_x(\text{As}_2\text{S}_3)_{1-x}$ pseudo-binaries with increasing x .⁷¹ Later, we will see that the 1.75 \AA^{-1} feature corresponds to the principle peak PP_{Sb} in the Sb-Sb partial structure factor $S_{\text{SbSb}}(Q)$, diverging from that in the $S_{\text{SS}}(Q)$ partial at $Q_{\text{S}} = 2.24 \text{ \AA}^{-1}$ because of a large difference in atomic size of antimony and sulfur, whose covalent radii are $r_{\text{Sb}} = 1.45 \text{ \AA}$ and $r_{\text{S}} = 1.03 \text{ \AA}$.^{93,94} The FSDP and PP_{Sb} are better visible after removing the background underneath the low- Q features using the subtraction procedure,^{95,96} Figure 6a.

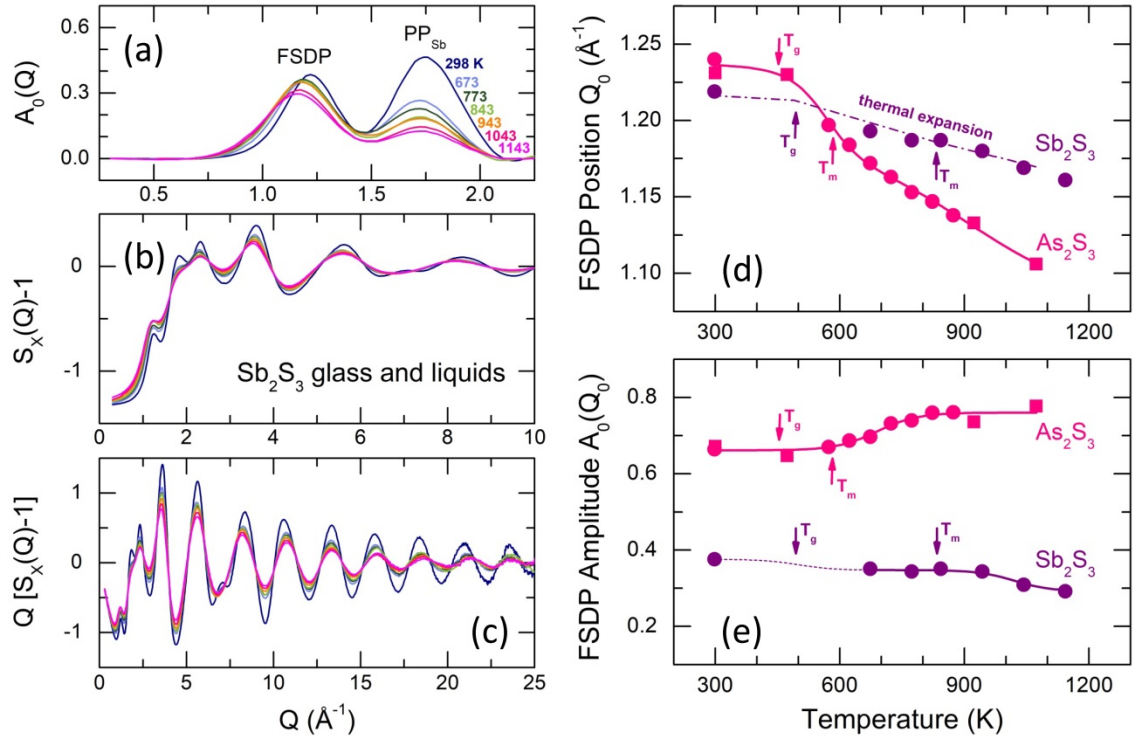


Figure 6. High-energy X-ray diffraction data in Q -space for glassy and liquid Sb_2S_3 : (a) isolated first sharp diffraction peak (FSDP) and Sb-Sb diffraction feature PP_{Sb} as a function of temperature; (b) X-ray structure factor $S_X(Q)$ over a limited Q -range and (c) interference function $Q[S_X(Q)-1]$ as a function of temperature; (d) the FSDP position $Q_0(T)$ and (e) amplitude $A_0(Q_0, T)$ for antimony and arsenic sesquisulfides. The dash-dotted line for Sb_2S_3 in (d) shows the expected $Q_0(T)$ trend taking into account the thermal expansion. The arrows show the glass transition temperature T_g and melting point T_m for As_2S_3 and Sb_2S_3 . The solid and dashed lines in (d) and (e) are a guide to the eye.

The FSDP amplitude $A_0(Q_0)$ slightly decreases in intensity with increasing T and shifts to lower Q , Figure 6a. In contrast, changes in the PP_{Sb} amplitude are more significant (especially between the solid glass and liquids) and similar to other peaks and distant oscillations, Figure 6b,c. In addition, these temperature changes are characteristic for chalcogenide glasses and liquids, while the FSDP behaves differently. Comparison with canonical As_2S_3 reveals both a common trend and a dissimilarity, Figure 6d,e. In particular, the FSDP position $Q_0(T)$ for Sb_2S_3 follows the thermal expansion, $Q_0(T) \propto \rho(T)^{1/3}$,⁹⁷ where $\rho(T)$ is the macroscopic number density, while $Q_0(T)$ for As_2S_3 is not. We will discuss this topic later.

The X-ray total correlation functions $T_X(r)$ for glassy and liquid Sb_2S_3 , obtained by the usual Fourier transform of $S_X(Q)$, are shown in Figure 7. The first peak at 2.484 ± 0.004 Å corresponds to Sb-S nearest neighbors followed by a strongly asymmetric second neighbor (2^{nd}N) peak at 3.83 ± 0.02 Å with additional unresolved correlations between 2.8 and 3.4 Å. The third distinct feature at 5.7 Å seems to be related to a center-center distance between the Sb-S entities. All peaks become less intense and broader with increasing temperature, also leading to a stronger overlapping between NN and second neighbor correlations. More distant broad peaks at 7.3 and 9 Å appear to be hardly visible in $L\text{-Sb}_2\text{S}_3$. Gaussian fitting of the NN and 2^{nd}N correlations is inappropriate because of the peak asymmetry. Typical fitting with asymmetric functions is shown in Figure 7a and yields reasonable results. The average antimony coordination $N_{\text{Sb-X}}$, where $X = \text{S}$ and/or Sb , was found to be trigonal and consisting of two contributions,

$N_{\text{Sb-X}} = N_{\text{Sb-S}} + N_{\text{Sb-Sb}} = 2.90(5) + 0.10(5)$, Figure 7c (see also Table 1). The Sb-S and Sb-Sb NN distances slightly increase with temperature; the both interatomic separations, $r_{\text{Sb-S}} = 2.484 \pm 0.004$ Å and $r_{\text{Sb-Sb}} = 2.92 \pm 0.02$ Å, are consistent with crystalline and amorphous references for trigonal antimony sulfides and elemental Sb.^{16-18,93,98} Typical broadening of the Sb-S NN feature as a function of temperature is shown in Figure 7f. Both supercooled and normal liquids Sb_2S_3 exhibit a monotonic increase of $w_{\text{Sb-S}}(T)$.

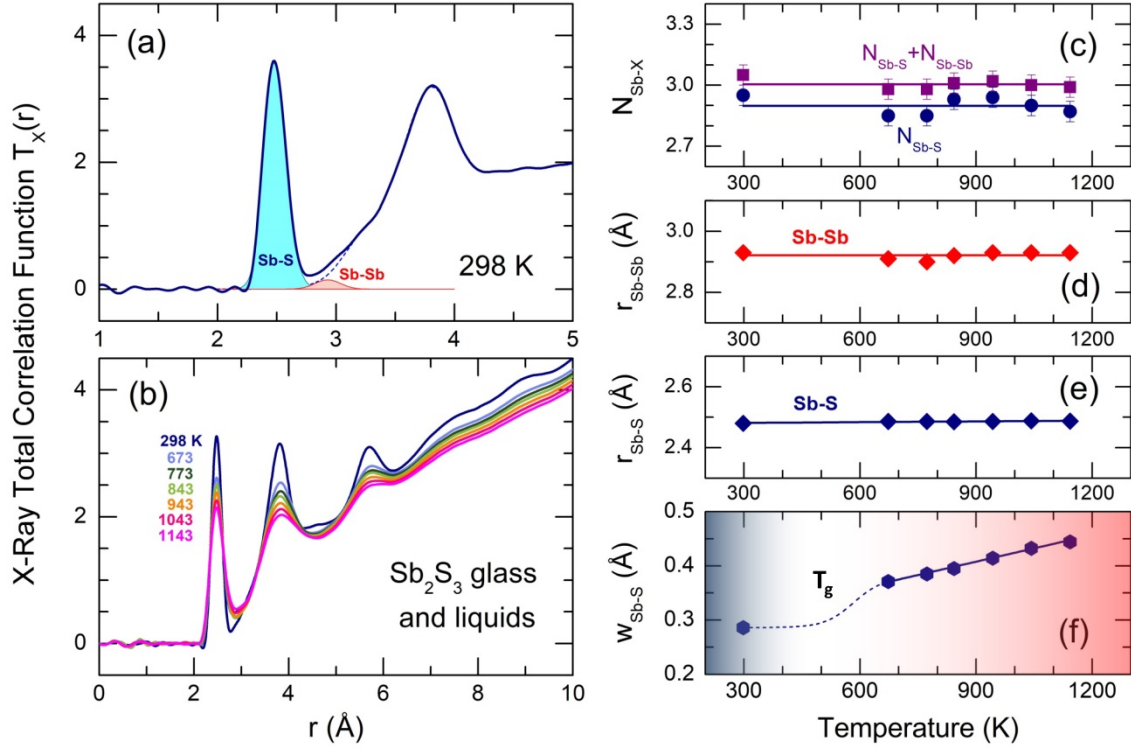


Figure 7. High-energy X-ray diffraction data in r -space for glassy and liquid Sb_2S_3 : (a) typical $T_X(r)$ fitting with asymmetric functions; Sb-S and Sb-Sb nearest neighbor (NN) correlations are highlighted in cyan and light red, respectively; (b) total correlation functions $T_X(r)$ over the temperature range $298 \leq T \leq 1143$ K; (c) antimony local coordination number as a function of temperature; (purple squares) $N_{\text{Sb-S}} + N_{\text{Sb-Sb}}$, (dark blue circles) $N_{\text{Sb-S}}$; interatomic NN distances (d) Sb-Sb and (e) Sb-S as a function of T ; (f) temperature dependence of asymmetric peak width for Sb-S NN correlations $w_{\text{Sb-S}}$; the solid glass and supercooled or normal liquid temperature domains are highlighted in blue and red, respectively. The dashed line in (f) is a guide to the eye. The other solid lines are a least-square fit of the experimental data.

3.5. First-Principles Molecular Dynamics Modeling of Glassy and Liquid Sb_2S_3 . The derived FPMD interference functions $Q[S_X(Q)-1]$ and pair-distribution functions $g_X(r)$ for the two extremes in experimental series at 300 and 1150 K are shown in Figure 8. As it was reported earlier,⁵⁶⁻⁵⁹ the FPMD with hybrid functional PBE0 yields a good agreement with experimental data for chalcogenide systems. The FPMD replicas in Q -space reproduce well both the positions and amplitudes of oscillations for $Q[S_X(Q)-1]$, Figure 8a,b. As a result, the derived interatomic distances in r -space are also consistent with the diffraction results, Figure 8c,d. In contrast, FPMD modeling with the standard functional PBE suffers from over- or underestimated correlations in Q - and r -space as it is shown in Figure S6.

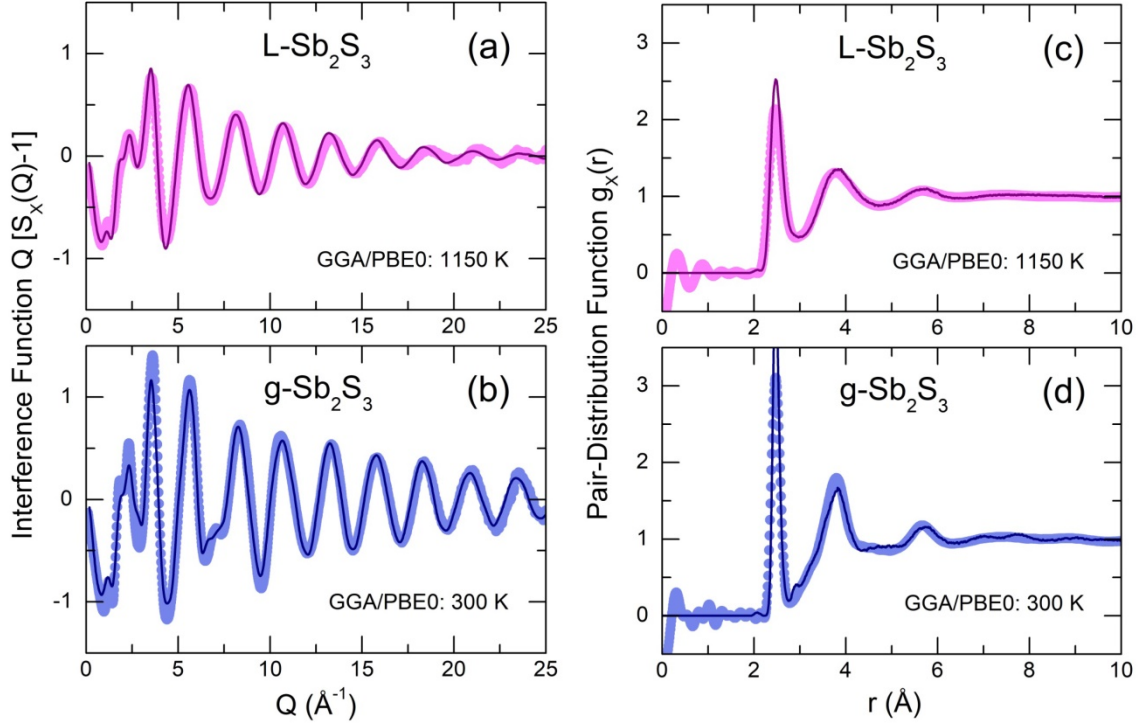


Figure 8. FPMD modeling results using hybrid functional GGA/PBE0 in comparison with experimental high-energy X-ray diffraction data for Sb_2S_3 ; interference function $Q[S_x(Q)-1]$ at (a) 1150 K and (b) 300 K; pair-distribution function $g_x(r)$ at (c) 1150 K and (d) 300 K. The solid circles correspond to experimental data; the solid lines are the FPMD results.

Table 1. Interatomic distances r_{ij} and partial coordination numbers N_{ij} in glassy and liquid Sb_2S_3 .

Temperature (K)	S-S		Sb-S		Sb-Sb	
	$r_{\text{S-S}}$ (\AA)	$N_{\text{S-S}}$	$r_{\text{Sb-S}}$ (\AA)	$N_{\text{Sb-S}}$	$r_{\text{Sb-Sb}}$ (\AA)	$N_{\text{Sb-Sb}}$
High-Energy X-Ray Diffraction						
298	—	—	2.480(6)	2.95(4)	2.93(2)	0.10(5)
673	—	—	2.486(6)	2.85(4)	2.91(2)	0.13(5)
773	—	—	2.486(6)	2.85(4)	2.90(2)	0.13(5)
843	—	—	2.485(6)	2.93(4)	2.92(2)	0.08(5)
943	—	—	2.486(6)	2.94(4)	2.93(2)	0.08(5)
1043	—	—	2.488(6)	2.90(4)	2.93(2)	0.10(5)
1143	—	—	2.487(6)	2.87(4)	2.93(2)	0.12(5)
First-Principles Molecular Dynamics						
300	2.07	0.07	2.471	2.93	2.90	0.10
700	2.07	0.08	2.474	2.88	2.90	0.12
800	2.07	0.08	2.478	2.89	2.90	0.12
850	2.07	0.08	2.478	2.92	2.91	0.12
950	2.07	0.08	2.482	2.91	2.91	0.13
1050	2.08	0.08	2.480	2.95	2.90	0.13
1150	2.07	0.08	2.478	2.94	2.90	0.13

The partial structure factors $S_{ij}(Q)$ and pair-distribution functions $g_{ij}(r)$ are revealed in Figure 9a,b. We note divergent positions of PP_{Sb} and PP_S for the $S_{SbSb}(Q)$ and $S_{SS}(Q)$ partials, as well as a negative amplitude of $S_{SbS}(Q)$ in this range, explaining the appearance of additional low- Q feature at $Q_{Sb} = 1.75 \text{ \AA}^{-1}$ in the X-ray structure factor discussed above, Figure 6a-c. Astonishingly, the FSDP origin appears to be related to Sb-S correlations instead of expected Sb-Sb counterparts. We note, however, that in glassy As_2S_3 , the FSDP origin changes from As-As (major contribution) and As-S (minor component) at ambient pressure to mostly As-S correlations above 4 GPa, Figure S7 in the Supporting Information.

The partial pair-distributions $g_{ij}(r)$ are consistent with experimental findings. The Sb-S NN peak at $2.477 \pm 0.004 \text{ \AA}$ exhibits an asymmetric shape, increasing with temperature, Figure S8. The fitting with asymmetric functions yields very similar results to the experimental data, $\langle N_{Sb-S} \rangle = 2.91 \pm 0.03$, and the antimony local trigonal coordination is completed by the Sb-Sb nearest neighbors at $2.903 \pm 0.002 \text{ \AA}$, $\langle N_{Sb-Sb} \rangle = 0.12 \pm 0.01$, Table 1. The Sb-S second neighbors are located rather close to the Sb-S NN correlations and overlap significantly with increasing temperature despite the shift of r_{Sb-S}^{2nd} to higher distances from 3.36 \AA (300 K) to 3.51 \AA (1150 K), mostly because of a strong broadening of the NN and 2ndN correlations, Figure S8.

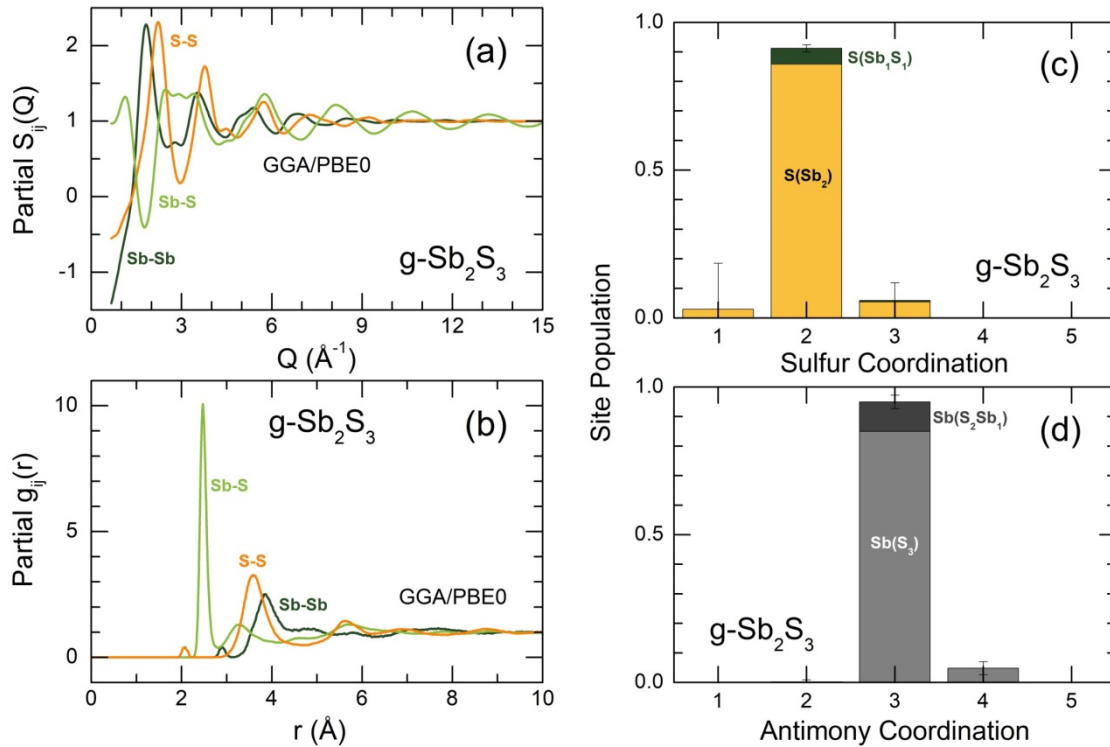


Figure 9. Derived FPMD partial functions for glassy Sb_2S_3 at 300 K in (a) Q -space, $S_{ij}(Q)$, and (b) r -space, $g_{ij}(r)$; and local coordination numbers for (c) sulfur, N_{S-X} , and (d) antimony, N_{Sb-X} , where $X = S$ or Sb .

The $g_{SS}(r)$ partial also shows S-S homopolar bonds at 2.07 \AA , Figure 9b, $\langle N_{S-S} \rangle = 0.08 \pm 0.01$, Table 1. The Raman spectroscopy confirms this result, Figure 4b. Nevertheless, their concentration is too low to be observed by high-energy X-ray diffraction. Figure 8c,d reveals that the S-S FPMD diffraction features are less intense compared to experimental noise of $g_X(r)$.

Sulfur and antimony coordination distributions are plotted in Figure 9c,d. As expected, the overwhelming majority of the two species have a two-fold (91%) and trigonal (95%) local

coordination, respectively. With increasing temperature, the population of two-fold sulfur and three-fold antimony decreases, while the fractions of under- and over-coordinated species grow, Figure S9. The number of sulfur or antimony local configurations with homopolar bonds, that is, $S(Sb_1S_1)$ instead of $S(Sb_2)$ or $Sb(S_2Sb_1)$ vs. $Sb(S_3)$ remains low at all temperatures.

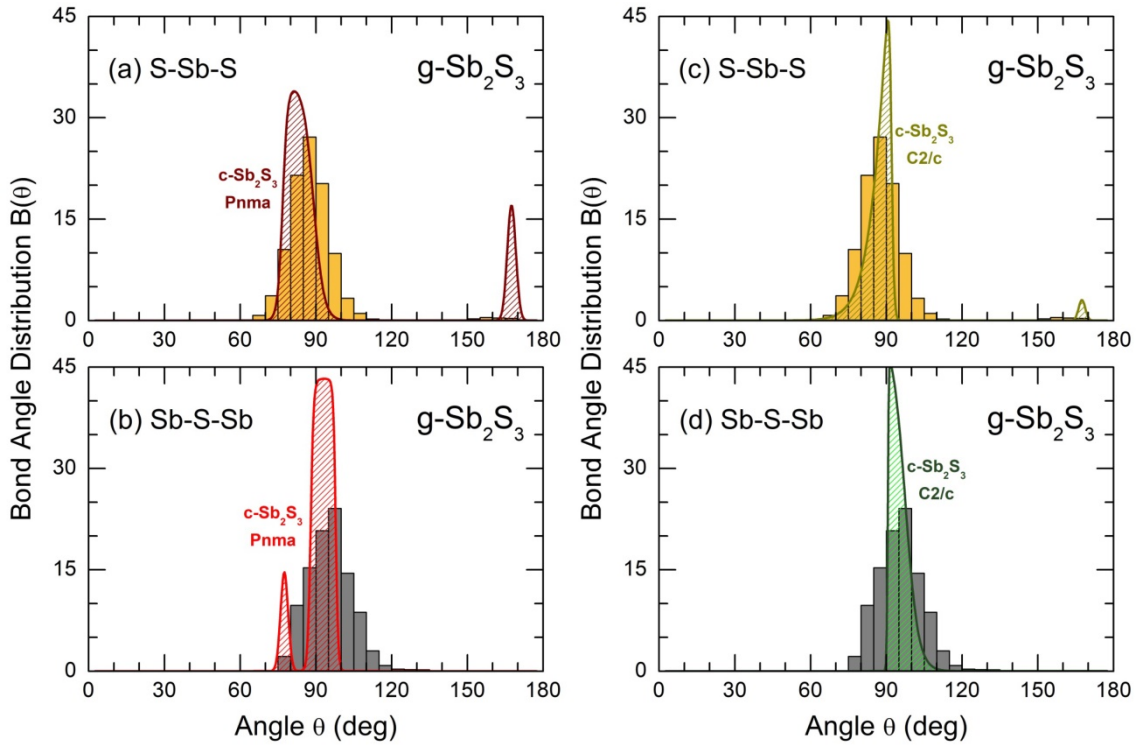


Figure 10. Bond angle distributions $B(\theta)$ for glassy Sb_2S_3 : (a) S-Sb-S and (b) Sb-S-Sb angles in comparison with orthorhombic Sb_2S_3 , space group $Pnma$;¹⁶ and (c) S-Sb-S and (d) Sb-S-Sb in comparison with monoclinic Sb_2S_3 , space group $C2/c$.¹⁸

The bond angle distributions $B(\theta)$ for S–Sb–S and Sb–S–Sb triplets in glassy Sb_2S_3 are plotted in Figure 10 in comparison with two crystalline counterparts: orthorhombic and monoclinic Sb_2S_3 . The geometry of SbS_3 trigonal pyramids is different from that in canonical $g\text{-As}_2S_3$; the maximum of a broad asymmetric distribution $B_{SSbS}(\theta)$ is located at 87° in opposite to 98° in arsenic sesquisulfide,⁹⁹ ensuring a more compact local structure of $g\text{-Sb}_2S_3$. Roughly speaking, SbS_3 pyramids can be considered as distorted defect octahedral entities, whose three missing Sb–S bonds became excessively long, and the corresponding sulfur species were transformed into the second neighbors. The above mentioned fitting of $T_{SbS}(r)$ partials, Figure S8, is consistent with this hypothesis, revealing three 2ndN correlations at ≈ 3.4 Å. The remnants of octahedral geometry are also evidenced by a weak contribution at $\theta \approx 160^\circ$. The $B_{SSbS}(\theta)$ distributions in orthorhombic and monoclinic polymorphs are rather similar to that in the glass, especially in the high-temperature $C2/c$ form, including a low-intensity component at $168 \pm 4^\circ$ of four-fold coordinated Sb(5)/Sb(6) species.¹⁶ The 5-fold coordinated Sb(II) atoms in orthorhombic Sb_2S_3 yield an intense contribution at $\theta \approx 171^\circ$.¹⁶

The connectivity of trigonal pyramids, reflected by $B_{SbSSb}(\theta)$ peaked at 97° , is also appeared to be in favor of more compact structure of glassy Sb_2S_3 compared to canonical $g\text{-As}_2S_3$. The $B_{AsSAs}(\theta)$ distribution in the latter has a maximum at 105° .⁹⁹ Crystalline Sb_2S_3 counterparts

exhibit similar connectivities to glassy antimony sesquisulfide, slightly less evident for the orthorhombic polymorph.

As expected, the supercooled and normal Sb_2S_3 liquids are characterized by even more distorted Sb-S polyhedra and polyhedral connectivities. Both $B_{\text{SbS}}(\theta)$ and $B_{\text{SbSSb}}(\theta)$ distributions become broader and less symmetric with increasing temperature, Figure S10.

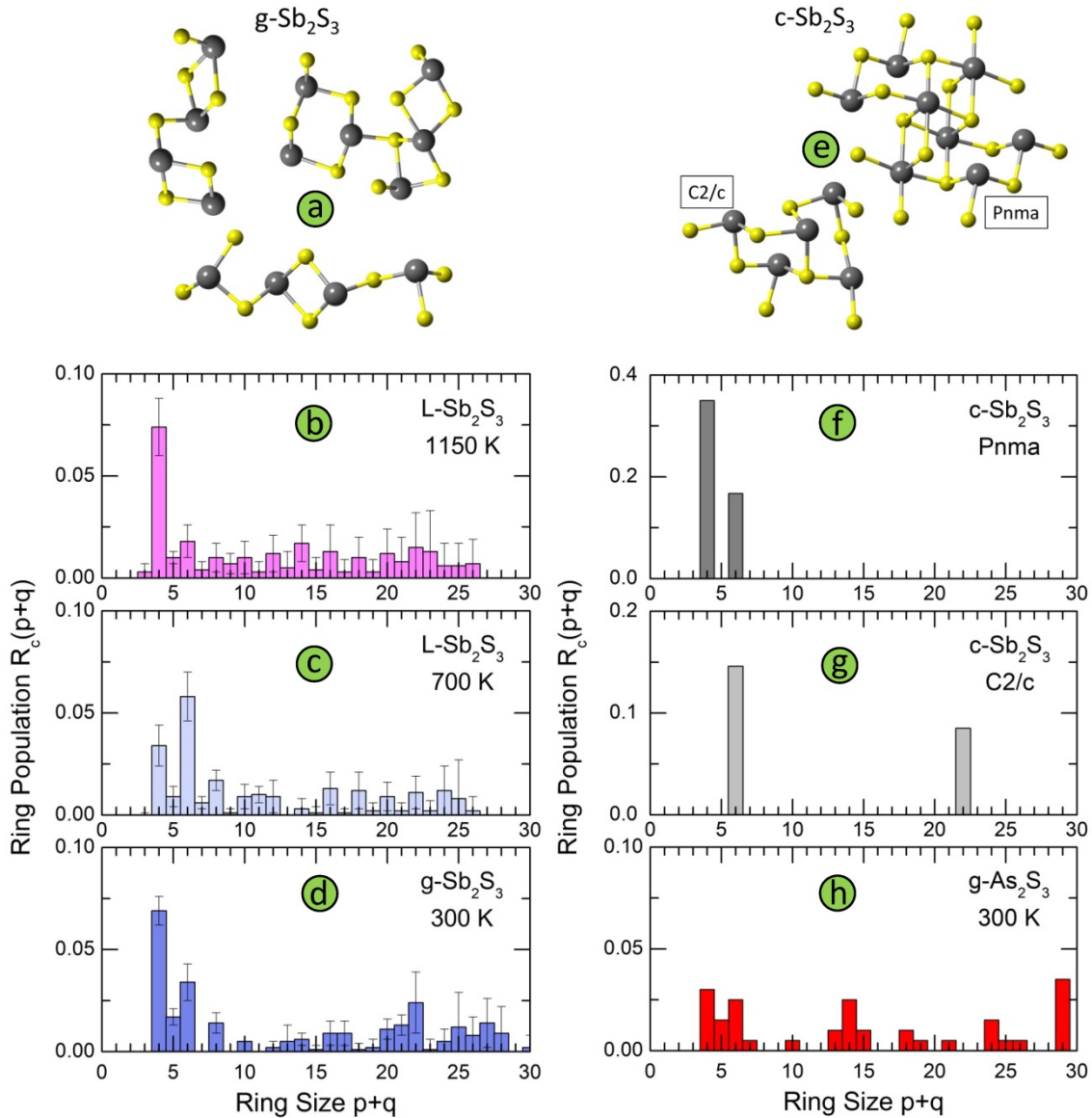


Figure 11. Structural motifs and ring statistics; (a) typical fragments in $g\text{-Sb}_2\text{S}_3$; ring statistics in glassy, and liquid Sb_2S_3 as a function of temperature: (b) 1150 K (normal liquid), (c) 700 K (supercooled liquid), and (d) 300 K (solid glass); (e) structural motifs in monoclinic Sb_2S_3 , space group $C2/c$,¹⁸ and orthorhombic Sb_2S_3 , space group $Pnma$;¹⁹ ring statistics in (f) orthorhombic Sb_2S_3 , (g) monoclinic Sb_2S_3 , and (h) glassy As_2S_3 .

The connectivity analysis shows that 96% of Sb and S are forming a single connected fragment. The homopolar bonds in the glass network are mostly related to few Sb-Sb and S-S dimers. Typical structural fragments in $g\text{-Sb}_2\text{S}_3$ are shown in Figure 11a. We note a certain similarity in the intermediate range order and ring statistics with orthorhombic and monoclinic polymorphs, Figure 11, expected from the bond angle distributions. The orthorhombic crystal has $ABAB$

squares (A : Sb; B : S) and six-membered rings Sb_3S_3 ; the monoclinic form, in addition to 6-fold entities, exhibits also big $\text{Sb}_{11}\text{S}_{11}$ rings, Figure 11g. Glassy and liquid Sb_2S_3 reveal a large variety of even- and odd-membered rings Sb_pS_q , $3 \leq p+q \leq 30$, related to chemical and topological disorder. Nevertheless, the most populated entities have size $p+q = 4$ and 6. The big rings, showing a broad distribution peaked at $p+q = 22$, become progressively unstable with increasing temperature. Their derived population $R_c(p+q)$ ⁶⁸ appears to be comparable with temporal fluctuations, reflected by the $R_c(p+q)$ uncertainty. At the highest temperature (1150 K), the population of $ABAB$ squares exceeds any other $R_c(p+q)$, at least, by a factor of 4, Figure 11b.

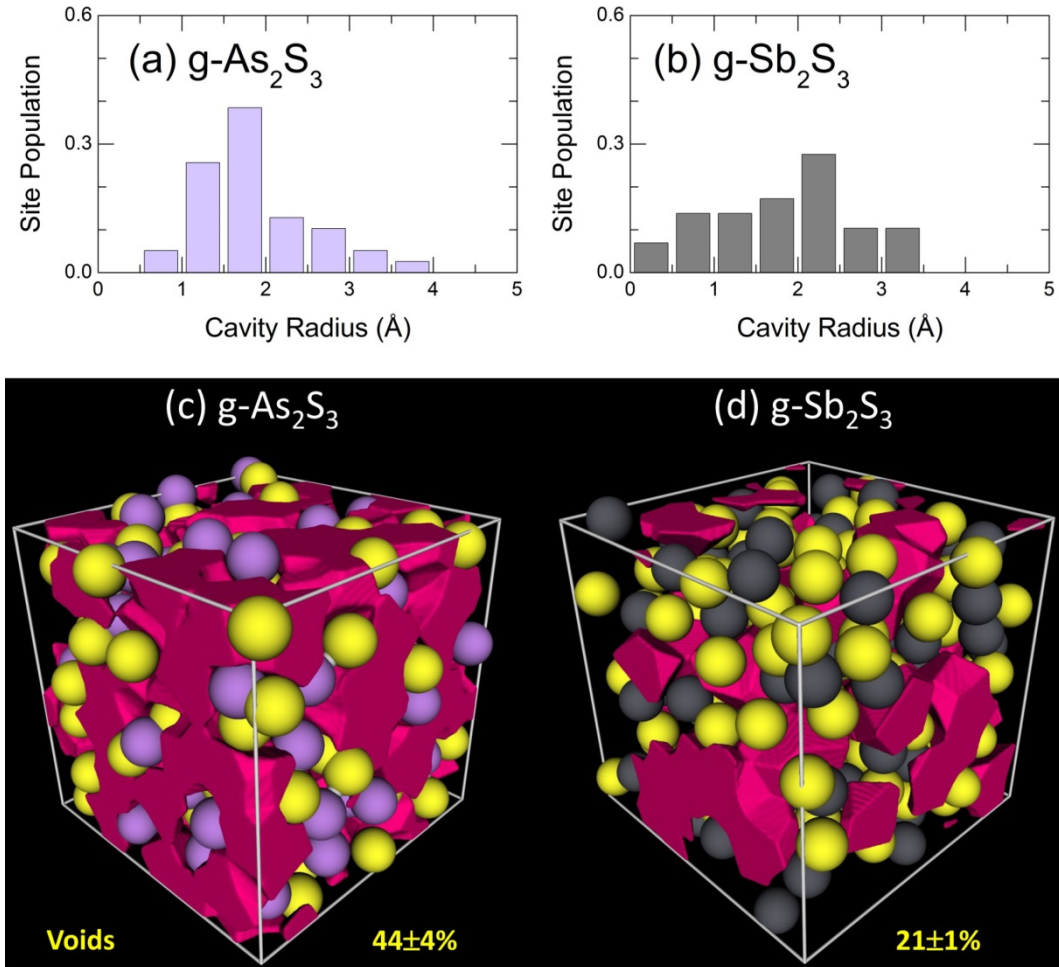


Figure 12. Void statistics: characteristic cavity radii in glassy (a) As_2S_3 and (b) Sb_2S_3 ; microscopic voids in (c) $g\text{-As}_2\text{S}_3$ and (d) $g\text{-Sb}_2\text{S}_3$.

The ring statistics in $g\text{-As}_2\text{S}_3$ is rather similar to that in glassy antimony sesquisulfide. As it was reported previously,⁹⁹ the 12-membered rings As_6S_6 , the only rings in monoclinic orpiment¹⁰⁰ and triclinic anorpiment¹⁰¹ As_2S_3 are absent in glassy arsenic sulfide, Figure 11h.

More dense packing of glassy antimony sesquisulfide, evidenced by bond angle distributions $B_{\text{SbSbS}}(\theta)$ and $B_{\text{SbSSb}}(\theta)$, suggests less microscopic voids and cavities in the glass network compared to $g\text{-As}_2\text{S}_3$. The Dirichlet-Voronoi tessellation⁷⁰ allows the cavity fraction V_c , normalized to the volume of the FPMD simulation box, $0 \leq V_c \leq 1$, to be computed. The results are given in Figure 12 for the two pnictide sesquisulfides. As expected, the V_c in $g\text{-Sb}_2\text{S}_3$ is by a

factor of two smaller than that of its arsenic counterpart, $21\pm1\%$ vs. $44\pm4\%$, respectively. The average size distribution of microscopic voids is rather similar in the two cases, $0.5 \leq r_c \leq 4 \text{ \AA}$, where r_c is the cavity radius, Figure 12a,b, although the average $\langle r_c \rangle$ is slightly smaller in glassy As_2S_3 .

In summary, glassy and liquid antimony sesquisulfide has distinctly different structural features compared to orthorhombic Sb_2S_3 . First, the antimony short range order in the crystal has a bimodal site distribution: 5-fold coordinated Sb(II) species with a strong Peierls distortion and regular trigonal Sb(I) entities. The Sb-S bonding asymmetry is absent in glassy and liquid polymorphs, characterized by a distorted antimony trigonal environment and shorter average $\langle r_{\text{Sb-S}}^{\text{NN}} \rangle$ distances, $2.64\pm0.15 \text{ \AA}$ ($c\text{-Sb}_2\text{S}_3$, $Pnma$) vs. $2.48\pm0.01 \text{ \AA}$ ($g\text{-}$ and $L\text{-Sb}_2\text{S}_3$). This difference is clearly seen by ^{121}Sb -Mössbauer spectroscopy,¹⁰² which is very sensitive to the local antimony environment.¹⁰³

Second, the intermediate range order in orthorhombic and glassy Sb_2S_3 is also different. The crystal structure is composed of infinite $1\text{D-(Sb}_4\text{S}_6)_\infty$ ribbons with rather strong inter-ribbon interactions, while the glass network has a 2D layered structure, roughly reminiscent of that in canonical As_2S_3 but with remarkable differences. We should note comparable glass transition temperatures for the two vitreous alloys, Figure 1, similar shape of the Raman spectra, Figure 4, identical pnictide and sulfur local coordination and resembling ring statistics. However, the topology of antimony defect octahedral sites SbS_3 , evidenced by bond angle distributions, is closer to crystalline Sb_2S_3 forms than to vitreous As_2S_3 .

3.6. Electronic Structure and Atomic Dynamics in Glassy and Liquid Sb_2S_3 . The total electronic density of states (eDOS), calculated from the Kohn-Sham eigenvalue spectra, is shown in Figure 13. The valence band (VB) consists of three sub-bands between the Fermi energy E_F and -20 eV , as in a large majority of crystalline and glassy chalcogenides.^{58,75,104-106} The upper asymmetric part, mostly involving sulfur and antimony p -electron populations, shows a predominant contribution at -2.8 eV ($g\text{-Sb}_2\text{S}_3$ at 300 K) or -2.3 eV ($L\text{-Sb}_2\text{S}_3$ at 1050 K), related to S $3p$ lone pairs. The bonding states at lower energies consist of Sb $5p$, $5d$ and $5s$ together with S $3p$ orbitals. The middle sub-band centered at -10.7 eV ($g\text{-Sb}_2\text{S}_3$) or -10.0 eV ($L\text{-Sb}_2\text{S}_3$) has predominantly the s -character as well as the low-energy part at approximately -15 eV . The bandgap for glassy ($E_g = 2.28 \text{ eV}$) and liquid ($E_g = 1.06 \text{ eV}$) antimony sesquisulfide are consistent with the reported optical data^{1,76-79} and electrical measurements (Figure 2).

The derived eDOS is in good agreement with experimental data¹⁰⁷ and previously reported simulation results.^{22,106,108-110} We should however note that simulations with the standard functionals yield strongly underestimated bandgap (roughly by a factor of 2) in addition to insufficient agreement with the nearest and second neighbor correlations (see also Figure S6).

The inverse participation ratio (IPR)^{104,111} (Figure 13a,d) characterizes the degree of localization of a single-particle Kohn-Sham eigenfunction $\psi(\mathbf{r})$

$$\text{IPR} = \frac{\int d\mathbf{r} |\psi(\mathbf{r})|^4}{(\int d\mathbf{r} |\psi(\mathbf{r})|^2)^2}. \quad (4)$$

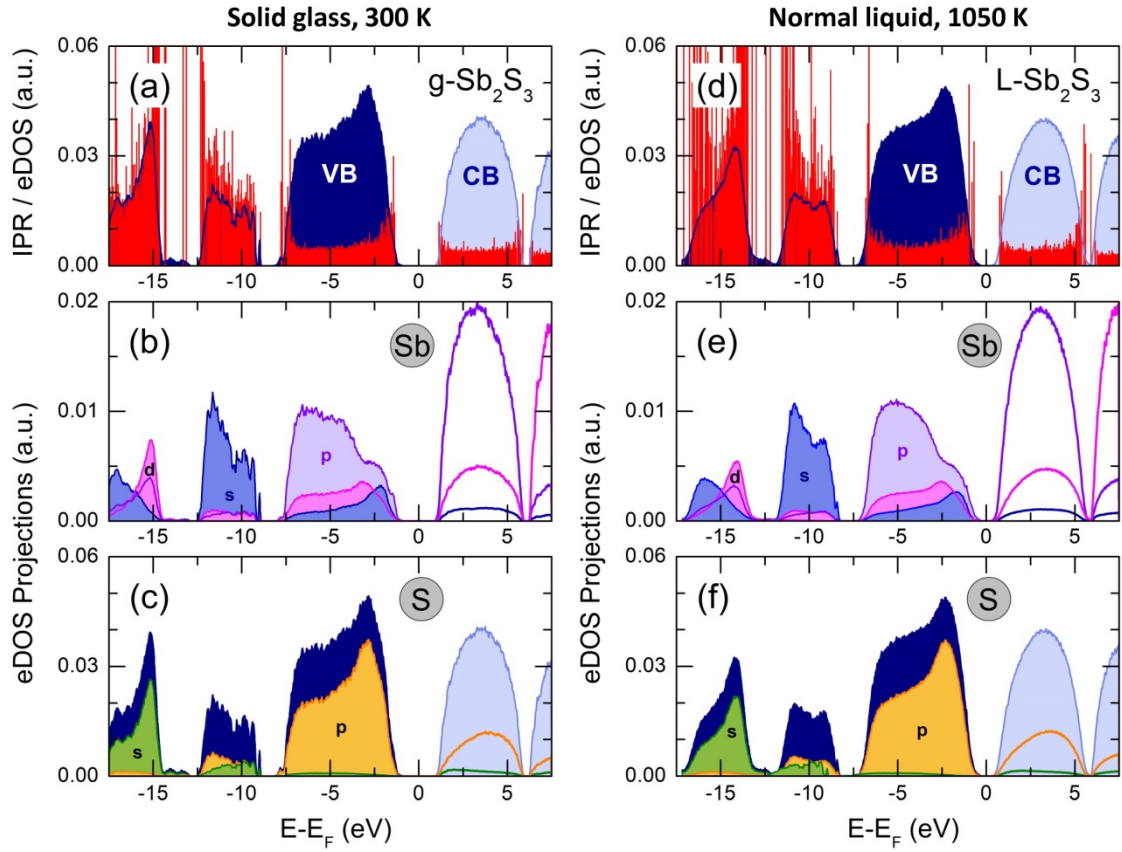


Figure 13. Electronic properties of glassy and liquid Sb_2S_3 ; solid glass at 300 K: (a) the electronic density of states (eDOS) and the inverse participation ratio (IPR, red spikes), the projected eDOS (pDOS) on (b) antimony s (blue), p (violet), and d (magenta), and (c) sulfur s (green) and p (yellow) pseudo-wave functions; normal liquid at 1050 K: (d) eDOS and IPR, (e) antimony pDOS, (f) sulfur pDOS. The valence band (VB) is highlighted in dark blue, the conduction band (CB) in light blue. See text for further details.

A small IPR value ($\propto N^{-1}$, where N is the number of atoms in the simulation box) corresponds to an extended (delocalized) wave function, while a large IPR ($\lim \text{IPR} \rightarrow 1$) indicates a strong localization around specific covalent bond. Similar to previously reported results^{58,104,111} and theoretical predictions,⁷⁵ the electron states in glassy and liquid Sb_2S_3 are mostly localized at the band tails (that is, the top of the valence and the bottom of the conduction bands) and in lower-lying bonding states. The remaining electron states in the vicinity of the bandgap are delocalized.

Benchmark telluride PCMs are characterized by low viscosity and high fragility of the melt¹¹²⁻¹¹⁶ ensuring fast atomic mobility at elevated temperature, which enables a rapid crystallization within the nanosecond range, and a good retention of amorphous phase in the vicinity of T_g and at lower T . The simulated dynamics in Sb_2S_3 reveals fast diffusion at high temperatures and a sudden decrease of diffusivity approaching the glass transition.

Typical Sb and S mean square displacements $\langle r^2(t) \rangle$ are shown in Figure 14a,b

$$\langle r^2(t) \rangle = \left\langle \frac{1}{N_i} \left\{ \sum_{i=1}^{N_i} [r_i(t) - r_i(0)]^2 \right\} \right\rangle, \quad (5)$$

where $r_i(0)$ and $r_i(t)$ are the positions of particle i for the initial time and time t , respectively, N_i the total number of particles i in the simulation box, and the angle brackets represent the

average over initial times. Below 30 fs, a ballistic regime is observed, mostly depending on atomic mass m_i ¹¹⁷

$$\langle r^2(t) \rangle \propto (k_B T / m_i) t^2, \quad (6)$$

where k_B and T are the Boltzmann constant and temperature. On a log-log scale, the slope $s = 2$ is indicative of this regime, Figure 14b.

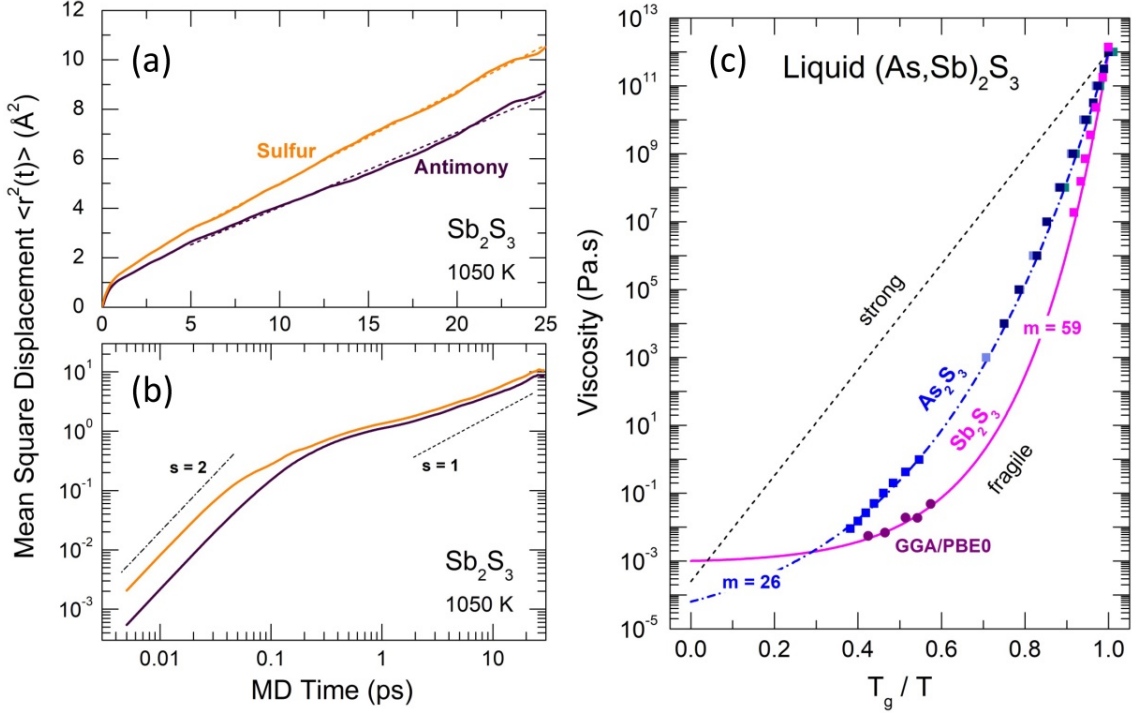


Figure 14. Mean-square displacements $\langle r^2(t) \rangle$ and viscosity of Sb_2S_3 . Antimony (dark purple) and sulfur (yellow) $\langle r^2(t) \rangle$ on (a) linear and (b) log-log scales. The dashed lines in (a) represent least-square fits of the $\langle r^2(t) \rangle$ data. The ballistic ($s = 2$) and diffusion ($s = 1$) regimes in (b) are shown by the dash-dotted and dashed lines, respectively. (c) Angell plot for the temperature dependence of viscosity $\eta(T)$ for As_2S_3 (blue) and Sb_2S_3 (magenta). The experimental viscosity data¹¹⁸⁻¹²³ are shown by the solid squares of different shades of blue for As_2S_3 , and by the magenta squares for Sb_2S_3 . The FPMD viscosity calculated using the Stokes–Einstein relation (eq 9) is shown by the purple circles (this work). The dashed-dotted and solid lines represent the MYEGA¹²⁴ viscosity (eq 10) for the two sesquisulfides. The derived fragility indices m are also shown. See the text for further details.

Above 5 ps, a diffusive motion is visible

$$\langle r^2(t) \rangle \propto D_i t, \quad (7)$$

where D_i is the average diffusion coefficient of particles i , approaching the slope $s = 1$. The diffusion coefficients D_{Sb} and D_{S} were calculated using the Einstein equation

$$D_i = \frac{1}{6} \lim_{t \rightarrow \infty} \frac{\partial \langle r_i^2(t) \rangle}{\partial t}. \quad (8)$$

The derived $D_{\text{Sb}}(T)$ and $D_{\text{S}}(T)$ are shown in Figure S11, plotted on Arrhenius scale and following thermally activated motion with temperature-dependent activation energy, $0.37 \leq E_d \leq 1.02$ eV in the vicinity of 1150 and 850 K, respectively.

The Stokes-Einstein relation was used to calculate the FPMD viscosity

$$\eta^{\text{FPMD}}(T) = \frac{k_B T}{6\pi D_{\text{eff}}(T) r_H}, \quad (9)$$

where the effective atomic diffusion coefficient $D_{\text{eff}}(T) = 0.4D_{\text{Sb}}(T) + 0.6D_{\text{S}}(T)$, and the effective temperature-dependent hydrodynamic radius r_H was determined using a Wigner-Seitz approach $r_{\text{WS}}(T) = \sqrt[3]{(3/4\pi)V_m(T)N_A^{-1}}$, where $V_m(T)$ is the melt molar volume and N_A the Avogadro constant.

The derived viscosity is shown using an Angell plot, $\log \eta$ vs. T_g/T (Figure 14c), together with experimental viscosity data of different research groups for canonical As_2S_3 and Sb_2S_3 .¹¹⁸⁻¹²³ The antimony sesquisulfide viscosity was obtained by extrapolation of the $(\text{GeS}_2)_x(\text{Sb}_2\text{S}_3)_{1-x}$ data, $0.1 \leq x \leq 0.9$.¹²³ At low $x \leq 0.5$, the $\log \eta(T, x)$ composition dependence is changing smoothly, enabling a reliable extrapolation of $\log \eta(T, x)$ to $x = 0$.

The both viscosities, $\eta(\text{As}_2\text{S}_3)$ and $\eta(\text{Sb}_2\text{S}_3)$, follow the Mauro-Yue-Ellison-Gupta-Allan (MYEGA) relationship¹²⁴ but with different fragilities

$$\log \eta(T) = \log \eta_0 + [\log \eta(T_g) - \log \eta_0] \frac{T_g}{T} \exp \left[\left(\frac{m}{\log \eta(T_g) - \log \eta_0} \right) \left(\frac{T_g}{T} - 1 \right) \right], \quad (10)$$

where the fragility index $m = [\partial \log \eta / \partial (T_g/T)]_{T=T_g}$, η_0 and $\eta(T_g) = 10^{12}$ Pa·s are the viscosity values at $T = \infty$ and T_g , respectively. The $m(\text{As}_2\text{S}_3) = 26$ is typical for canonical chalcogenide glasses with a network structure.^{113-116,125,126} Antimony sesquisulfide exhibits a higher fragility, $m(\text{Sb}_2\text{S}_3) = 59$, approaching that of telluride PCMs.¹¹³⁻¹¹⁶ We should also note a good agreement between experimental $\eta(T)$ and calculated $\eta^{\text{FPMD}}(T)$ viscosity.

We do not expect for Sb_2S_3 either a fragile-to-strong transition¹¹²⁻¹¹⁵ or mesoscopic immiscibility accompanied by a viscosity anomaly^{116,127} since both the experimental conductivity (Figure 2) and FPMD simulations (Figure 13) reveal a semiconducting behavior over the studied temperature range.

3.7. Sb_2S_3 and Other Sulfides of Group 15. The comparison with phosphorus, arsenic and bismuth sulfides allows better the atomic structure and dynamics of liquid and glassy Sb_2S_3 to be understood. Vitreous sulfides of group 15 reveal a distinct loss of molecular-like atomic structure with increasing atomic number. Phosphorus sulfides mostly exist in the form of cages P_4S_n , $3 \leq n \leq 10$ (see, for example, Ref 128 and references therein), and glasses in the system P_xS_{1-x} have a network structure essentially below $x \lesssim 0.20$ as a mixture of polymerized $\text{S}=\text{PS}_3$ tetrahedra (main entities), P_4S_{10} and P_4S_9 cages, sulfur rings and chains.^{129,130} Above this limit, the structure of glasses or viscous liquids at room temperature becomes increasingly dominated by P_4S_{10} ($x = 0.2857$), P_4S_9 , P_4S_7 and other P-rich cages,¹³⁰⁻¹³² that is, appears to be mostly molecular. The network-forming PS_3 trigonal pyramids possibly exist but as a minor contribution.

Arsenic sesquisulfide has a network structure both in crystalline^{100,101} and glassy forms. Nevertheless, the vapor over As_2S_3 , albeit quite complex,^{133,134} basically consists of As_4S_4 and other cages, which are also frozen in amorphous thin films obtained by thermal evaporation.¹³⁵⁻¹³⁷ Annealed evaporated As_2S_3 evolves into a polymeric structure similar to that in bulk g -

As₂S₃.¹³⁵⁻¹³⁹ In contrast, antimony and bismuth sulfide cages are unknown,¹⁴⁰ and Sb₂S₃ or Bi₂S₃ have a network structure composed of 1D-(Pn₄S₆)_∞ ribbons, where Pn = Sb, Bi.^{16,17,141}

The FSDP trends for arsenic and antimony sesquisulfides show a distinct difference, Figure 6d,e. In liquid Sb₂S₃, the FSDP position $Q_0(T)$ follows the thermal expansion, while $Q_0(T)$ in supercooled and normal liquid As₂S₃ reveals a strong deviation from the expected behavior going to much lower Q_0 values, Figure 15. The observed trend is reminiscent of that in amorphous evaporated As₂S₃ on annealing at T_g ^{138,139} but occurring in the opposite direction. The latter phenomenon was attributed to a polymerization of As₄S₄ cages in the as-deposited As₂S₃ films, confirmed also by Raman scattering,¹³⁵⁻¹³⁷ whereas in *L*-As₂S₃, there is a dissociation reaction $2\text{As-S} \rightleftharpoons \text{As-As} + \text{S-S}$ with a possible network fragmentation and changes in the intermediate range order. Tanaka¹⁴² was first to observe changes in the chemical and intermediate range order in *g*-As₂S₃ quenched from different temperatures, which are consistent with the observed trend in $Q_0(T)$, but also with an increasing FSDP amplitude $A_0(Q_0)$, Figure 6e.

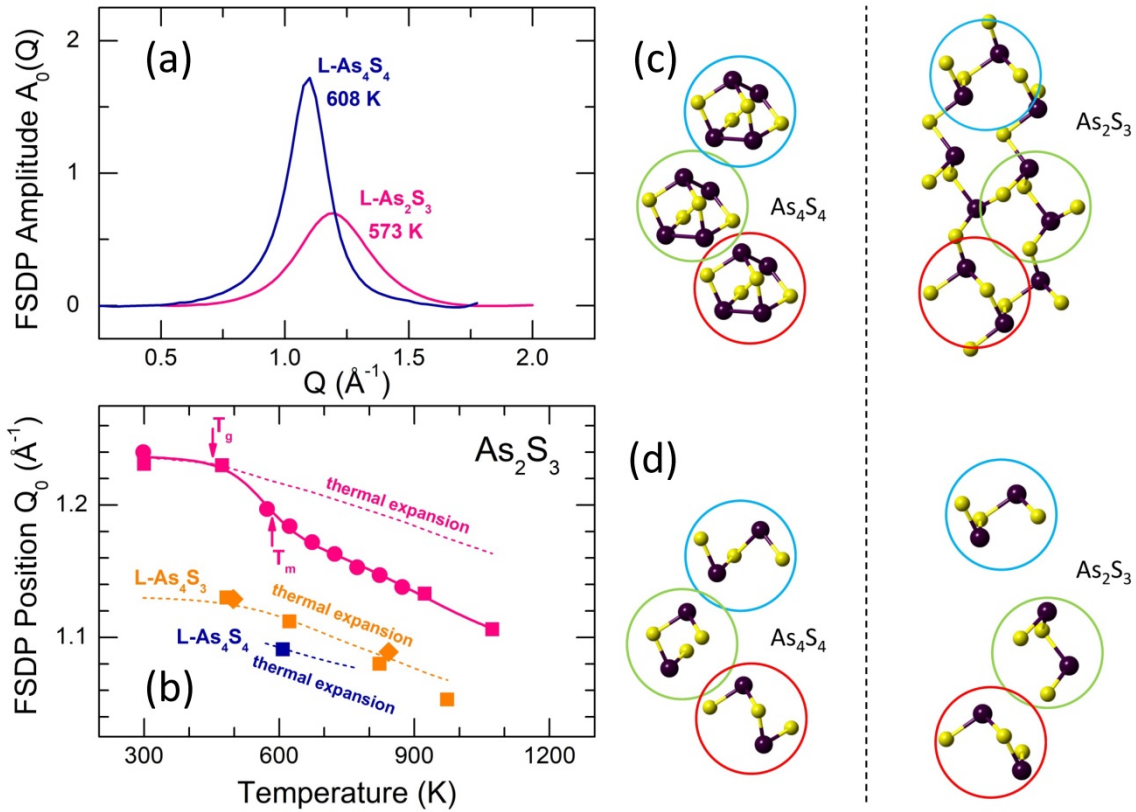


Figure 15. FSDP trends in liquid As₂S₃, As₄S₄ and As₄S₃; (a) isolated FSDPs in *L*-As₂S₃ at 573 K and *L*-As₄S₄ at 608 K; (b) FSDP positions $Q_0(T)$ for As₂S₃, As₄S₄ and As₄S₃ as a function of temperature; the dashed lines show the expected behavior taking into account the thermal expansion of arsenic sulfides; (c) specific projections of monoclinic orpiment As₂S₃ and realgar As₄S₄ to show their structural similarities; (d) nearly identical structural fragments are highlighted by the red, light green and light cyan circles for the two compounds.¹⁰⁰

Our preliminary high-temperature Raman measurements and FPMD modeling are also coherent with these observations as well as the FSDP parameters for liquid As₄S₃ and As₄S₄ as a function of temperature, Figure 15b. Reversible polymerization or depolymerization seems to be related to a striking resemblance of the interatomic distances and bond angles in the realgar As₄S₄ and

orpiment As_2S_3 crystal structures, noted by Ito¹⁴³, despite an apparent dissimilarity between the As_4S_4 cages and the As_2S_3 layered network.^{100,143} Schematically, the elements of conversion are shown in Figure 15cd, illustrating the idea that the two structures are built by nearly identical structural fragments connected differently.¹⁴³

Usually, the electronic conductivity increases and bandgap decreases going down on the Periodic Table. Vitreous, crystalline and liquid As_2S_3 and Sb_2S_3 are consistent with this trend. The room temperature conductivity of $g\text{-Sb}_2\text{S}_3$ is higher by three orders of magnitude compared to arsenic sesquisulfide, and the difference in E_g is about $\Delta E_g \approx 0.3$ eV. A semiconductor – metal (SC–M) transition is suggested to occur in these two high- T liquids. Using the extrapolation of the optical absorption data,¹⁴⁴ the SC–M transition is expected at $T_{\text{SC–M}} = 1600 \pm 150$ K for $L\text{-As}_2\text{S}_3$ ¹¹⁴ and between 1250 and 1550 K for its antimony counterpart. The last estimation was based on FPMD modeling of the bandgap as a function of temperature or derived from the computed atomic diffusion coefficients, Figure 16.

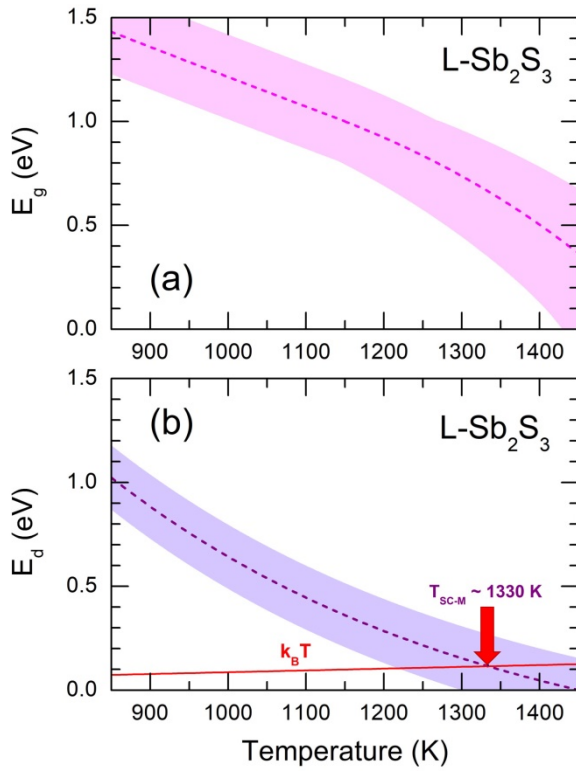


Figure 16. FPMD estimation of the SC–M transition temperature $T_{\text{SC–M}}$ for liquid Sb_2S_3 ; (a) bandgap E_g as a function of temperature; (b) atomic diffusion activation energy E_d as a function of temperature. The average thermal energy $k_B T$ is also shown in (b). The effective diffusion coefficient $D_{\text{eff}} = 0.4D_{\text{Sb}} + 0.6D_{\text{S}}$ was taken for these calculations.

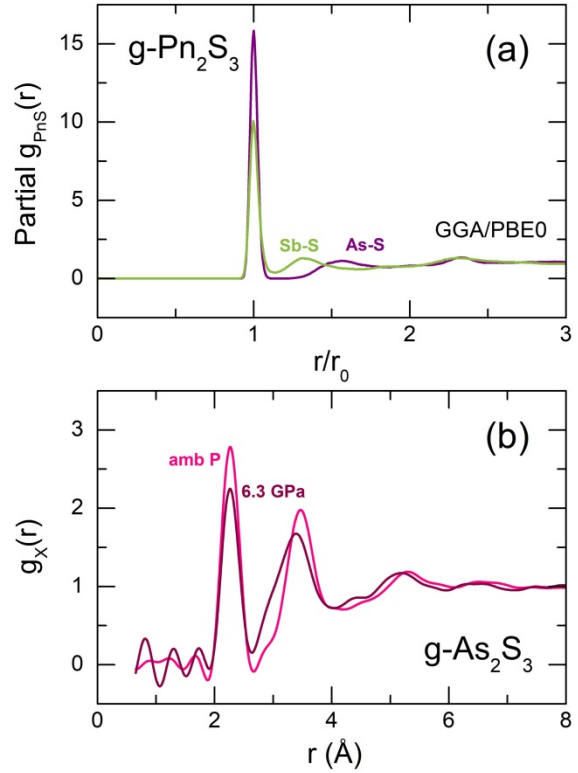


Figure 17. (a) FPMD partial pair-distribution functions $g_{\text{PnS}}(r)$ for $g\text{-Pn}_2\text{S}_3$, Pn = As, Sb; (b) experimental $g_X(r)$ for $g\text{-As}_2\text{S}_3$ at ambient pressure and 6.3 GPa;¹⁵⁰ broader NN and 2ndN peaks of $g_X(r)$ are related to a smaller accessible Q -range in a diamond anvil cell experiment, $Q_{\text{max}} = 16 \text{ \AA}^{-1}$ instead of usual 25–30 \AA^{-1} .

The bandgap calculations using the hybrid functional GGA/PBE0 in the metallic limit yields a significant uncertainty in $T_{\text{SC–M}} = 1550 \pm 120$ K. As expected, the modeling with the standard functional GGA/PBE reveals a metallic liquid at lower temperature, 1250 ± 75 K. The derived $T_{\text{SC–M}}$ values seem to be the two extremes for estimation of a SC–M transition using the electronic properties. Another alternative gives the atomic dynamics suggesting that the diffusion activation energy E_d in the metallic fluid appears to be comparable with the average

thermal energy, $E_d \approx k_B T$. This alternative yields $T_{SC-M} = 1330 \pm 100$ K, which corresponds to a change in the slope of $E_g(\text{PBE0})$, Figure 16a. Finally, liquid Sb_2S_3 exhibits the metallic conductivity above approximately 1300-1500 K.¹⁴⁵

We should also note a lower SC-M transition temperature, $900 \text{ K} \lesssim T_{SC-M} \lesssim 1100 \text{ K}$, for liquid antimony selenides.^{114,145} In addition, anionic (Se) or cationic (Bi) substitution can be used for bandgap engineering, since $E_g(\text{Sb}_2\text{Se}_3) = 1.0\text{--}1.3 \text{ eV}$ ^{12,146} and $E_g(\text{Bi}_2\text{S}_3) = 1.2\text{--}1.4 \text{ eV}$,^{147,148} remaining within the wider gap materials compared to tellurides, $E_g(\text{Sb}_2\text{Te}_3) = 0.5 \text{ eV}$.¹⁴⁹

Another general trend resides in a more compact or densified network for vitreous sulfides with increasing atomic number. We have already mentioned that the bond angle distributions $B_{SSbS}(\theta)$ and $B_{SbSSb}(\theta)$ as well as the lower fraction of microscopic voids and cavities in $g\text{-Sb}_2\text{S}_3$, Figures 10 and 12, are illustrating this trend. A comparison of the two partial pair-distribution functions $g_{PnS}(r)$ for $g\text{-As}_2\text{S}_3/\text{Sb}_2\text{S}_3$ seems to be even more convincing. Plotted on the normalized r/r_0 scale, where r_0 is the Pn-S NN distance, the $g_{SbS}(r)$ shows a remarkable shift of the Sb-S second neighbors to shorter distances, approaching the NN shell, Figure 17a. The observed more compact network compared to $g\text{-As}_2\text{S}_3$ at ambient conditions can be reproduced under high pressure. Figure 17b reveals a similar shift of the second neighbors for $g\text{-As}_2\text{S}_3$ in a diamond anvil cell at 6.3 GPa.¹⁵⁰ Comparable trends are observed in other groups of the Periodic Table, e.g. amorphous and liquid Se and Te, Figure S12.^{95,151-153} For liquid tellurium, a densification of the Te network is amplified by the SC-M transition in supercooled tellurium.^{75,114}

4. CONCLUDING REMARKS

Summarizing the above observations, we can emphasize favorable features in the atomic structure and dynamics of vitreous and liquid Sb_2S_3 as a promising next-generation PCM for integrated smart photonics from the visible to telecom window. A high optical and electric contrast between the SET and RESET logic states in antimony sesquisulfide is based on a different short and intermediate range order in orthorhombic and amorphous Sb_2S_3 . The orthorhombic polymorph is composed of quasi 1D- $(\text{Sb}_4\text{S}_6)_\infty$ ribbons with a strong asymmetry of the Sb-S nearest neighbor distances for three-fold and 5-fold antimony species ($2.46 \leq r_{\text{Sb-S}}^{\text{NN}} \leq 2.85 \text{ \AA}$) and significant inter-ribbon interactions. Glassy Sb_2S_3 reveals a 2D-disordered network built by defect octahedral entities SbS_3 ($r_{\text{Sb-S}}^{\text{NN}} = 2.48 \pm 0.01 \text{ \AA}$), whose three missing Sb-S bonds became excessively long, and the respective sulfur atoms were transformed into the second neighbors at $\approx 3.4 \text{ \AA}$. More compact network structure of $g\text{-Sb}_2\text{S}_3$ compared to canonical As_2S_3 , evidenced by the bond angle distributions, shorter Sb-S second neighbor distances and a lower population of microscopic voids and cavities, appears to be a good compromise between the stability of the amorphous state and the ability to fast crystallization. An additional positive feature is related to the intermediate range structure of liquid Sb_2S_3 , predominantly composed of *ABAB* squares, which are speeding up the crystallization phenomena. Another favorable aspect for the rapid SET-RESET transition is an enhanced fragility of liquid Sb_2S_3 . The fragility index $m = 59$ is approaching those of the benchmark telluride PCMs and enables fast crystallization processes at elevated temperatures and simultaneously a remarkable slowdown in the vicinity of T_g , ensuring a good retention of the amorphous phase. Furthermore, anionic (Se) and/or cationic (Bi) substitution maybe used to decrease the temperature of a SC-M transition, thus

improving the dynamics of the SET-RESET change, and allowing bandgap engineering equally important for photonics and photovoltaics.

ASSOCIATED CONTENT

Supporting Information

The Supporting Information is available free of charge at <https://pubs.acs.org/doi>

Raman spectrum of amorphous antimony, evolution of Raman spectra for Sb_2S_3 as a function of temperature, DFT Raman spectra of size-limited clusters, S-Sb-S bond angle distributions for DFT-optimized clusters, distributions of Sb-S interatomic distances in DFT-optimized clusters, comparison of FPMD modeling with standard PBE and hybrid PBE0 functionals, FPMD modeling of glassy As_2S_3 under high-pressure, fitting Sb-S partials with asymmetric functions, coordination distributions of sulfur and antimony, bond angle distributions in glassy and liquid Sb_2S_3 , derived Sb and S diffusion coefficients plotted on Arrhenius scale, pair-distribution functions of liquid and amorphous selenium and tellurium, and supporting references (PDF)

AUTHOR INFORMATION

Corresponding Author

Eugene Bychkov – Laboratoire de Physico-Chimie de l'Atmosphère, Université du Littoral Côte d'Opale, 59140 Dunkerque, France; orcid.org/0000-0002-3292-1205; Phone: +33 328 658250; Email: Eugene.Bychkov@univ-littoral.fr; Fax: +33 328 658244

Authors

Mohammad Kassem – Laboratoire de Physico-Chimie de l'Atmosphère, Université du Littoral Côte d'Opale, 59140 Dunkerque, France; orcid.org/0000-0003-0512-0004

Chris J. Benmore – X-ray Science Division, Advanced Photon Source, Argonne National Laboratory, Argonne, Illinois 60439, United States; orcid.org/0000-0001-7007-7749

Andrey Tverjanovich – Institute of Chemistry, St. Petersburg State University, St. Petersburg 198504, Russia; orcid.org/0000-0002-0795-8188

Takeshi Usuki – Faculty of Science, Yamagata University, Yamagata 990-8560, Japan; orcid.org/0000-0002-4737-7708

Maxim Khomenko – ILIT RAS–Branch of the FSRC “Crystallography and Photonics” RAS, 140700 Shatura, Moscow Region, Russia

Daniele Fontanari – Laboratoire de Physico-Chimie de l'Atmosphère, Université du Littoral Côte d'Opale, 59140 Dunkerque, France

Anton Sokolov – Laboratoire de Physico-Chimie de l'Atmosphère, Université du Littoral Côte d'Opale, 59140 Dunkerque, France

Koji Ohara – Research and Utilization Division, Japan Synchrotron Radiation Research Institute, Sayo, Hyogo 679-5198, Japan; orcid.org/0000-0002-3134-512X

Maria Bokova – Laboratoire de Physico-Chimie de l’Atmosphère, Université du Littoral Côte d’Opale, 59140 Dunkerque, France

Shinji Kohara – Quantum Beam Field, Research Center for Advanced Measurement and Characterization, National Institute for Materials Science, 1–2–1 Sengen, Tsukuba, Ibaraki 305–0047, Japan; orcid.org/0000-0001-9596-2680

Complete contact information is available at: <https://pubs.acs.org/10.1021>

Author Contributions

The manuscript was written through contributions of all authors. All authors have given approval to the final version of the manuscript.

Notes

The authors declare no competing financial interest.

ACKNOWLEDGMENTS

This work was supported by the Région Hauts de France and the Ministère de l’Enseignement Supérieur et de la Recherche (CPER Climibio), as well as by the European Fund for Regional Economic Development. Work at the Advanced Photon Source, Argonne National Laboratory, was supported in part by the Office of Basic Energy Sciences, US Department of Energy, under Contract No. DE-AC02-06CH1135. The experiments at SPring-8 were approved by the Japan Synchrotron Radiation Research Institute (proposal Nos. 2021A1432 and 2022A1418) and supported by the Centre for Advanced Science and Technology (Japan). MKh work at ILIT RAS was supported by state assignment FSRC “Crystallography and Photonics”, Russian Academy of Sciences. This work was granted access to the HPC resources of IDRIS (France) under the allocation 2022-A0130910639 made by Grand Equipement National de Calcul Intensif (GENCI) and to use the CALCULCO computing platform, supported by Service COMMUN du Système d’Information de l’Université du Littoral Côte d’Opale (SCoSI/ULCO). The FPMD simulations were also carried out using the equipment of the shared research facilities of HPC computing resources at Lomonosov Moscow State University.

REFERENCES

- (1) Dong, W.; Liu, H.; Behera, J. K.; Lu, L.; Ng, R. J. H.; Sreekanth, K. V.; Zhou, X.; Yang, J. K. W.; Simpson, R. E. Wide Bandgap Phase Change Material Tuned Visible Photonics. *Adv. Funct. Mater.* **2018**, 1806181.
- (2) Delaney, M.; Zeimpekis, I.; Lawson, D.; Hewak, D. W.; Muskens, O. L. A New Family of Ultralow Loss Reversible Phase-Change Materials for Photonic Integrated Circuits: Sb_2S_3 and Sb_2Se_3 . *Adv. Funct. Mater.* **2020**, 2002447.
- (3) Liu, H.; Dong, W.; Wang, H.; Lu, L.; Ruan, Q.; Tan, Y. S.; Simpson, R. E.; Yang, J. K. W. Rewritable Color Nanoprints in Antimony Trisulfide Films. *Sci. Adv.* **2020**, 6, eabb7171.
- (4) Qin, S.; Xu, N.; Huang, H.; Jie, K.; Liu, H.; Guo, J.; Meng, H.; Wang, F.; Yang, X.; Wei, Z. Near-Infrared Thermally Modulated Varifocal Metalens Based on the Phase Change Material Sb_2S_3 . *Opt. Express* **2021**, 29, 7925–7934.
- (5) Lu, L.; Dong, Z.; Tijptoharsono, F.; Ng, R. J. H.; Wang, H.; Rezaei, S. D.; Wang, Y.; Leong, H. S.; Lim, P. C.; Yang, J. K. W.; Simpson, R. E. Reversible Tuning of Mie Resonances in the Visible Spectrum. *ACS Nano* **2021**, 15, 19722–19732.
- (6) Jia, W.; Menon, R.; Sensale-Rodriguez, B. Visible and Near-Infrared Programmable Multi-Level Diffractive Lenses with Phase Change Material Sb_2S_3 . *Opt. Express* **2022**, 30, 6808–6817.
- (7) Cao, L.; Gao, X.; Zhang, B.; Ou, X.; Zhang, J.; Luo, W.-B. Bimetallic Sulfide $\text{Sb}_2\text{S}_3/\text{FeS}_2$ Hollow Nanorods as High-Performance Anode Materials for Sodium-Ion Batteries. *ACS Nano* **2020**, 14, 3610–3620.
- (8) Wang, S.; Cheng, Y.; Xue, H.; Liu, W.; Yi, Z.; Chang, L.; Wang, L. Multifunctional Sulfur-Mediated Strategy Enabling Fast-Charging Sb_2S_3 Micro-Package Anode for Lithium-Ion Storage. *J. Mater. Chem. A* **2021**, 9, 7838–7847.
- (9) Chen, R.; Lu, X.; He, Q.; Yao, M.; Yao, T.; Gao, A.; Ding, S.; Cheng, Y.; Wang, H. Sb_2S_3 Nanorod Hierarchies Enabling Homogeneous Sodium Deposition for Dendrite-Free Sodium-Metal Batteries. *ACS Appl. Energy Mater.* **2022**, 5, 10952–10960.
- (10) Du, Y.; Liu, F.; Jiang, L.; Jia, M.; Zhang, Z. Ultra-Fine Sb_2S_3 Particles Encapsulated in Activated-Carbon: A High-Performance Anode for Li-ion Batteries. *J. Alloys Compd.* **2022**, 907, 164469.
- (11) Lian, W.; Jiang, C.; Yin, Y.; Tang, R.; Li, G.; Zhang, L.; Che, B.; Chen, T. Revealing Composition and Structure Dependent Deep-Level Defect in Antimony Trisulfide Photovoltaics. *Nat. Commun.* **2021**, 12, 3260.
- (12) Barthwal, S.; Kumar, R.; Pathak, S. Present Status and Future Perspective of Antimony Chalcogenide (Sb_2X_3) Photovoltaics. *ACS Appl. Energy Mater.* **2022**, 5, 6545–6585.
- (13) Roy, B.; Chakraborty, B. R.; Bhattacharya, R.; Dutta, A. K. Electrical and Magnetic Properties of Antimony Sulphide (Sb_2S_3) Crystals and the Mechanism of Carrier Transport in It. *Solid State Commun.* **1978**, 25, 937–940.
- (14) Chang, C.; Xiao, Y.; Zhang, X.; Pei, Y.; Li, F.; Ma, S.; Yuan, B.; Liu, Y.; Gong, S.; Zhao, L.-D. High Performance Thermoelectrics from Earth-Abundant Materials: Enhanced Figure of Merit in PbS through Nanostructuring Grain Size. *J. Alloys Compd.* **2016**, 664, 411–416.
- (15) Bao, D.; Sun, Q.; Huang, L.; Chen, J.; Tang, J.; Zhou, D.; Hong, M.; Yang, L.; Chen, Z.-G. Thermoelectric Performance of p-Type $(\text{Bi,Sb})_2\text{Te}_3$ Incorporating Amorphous Sb_2S_3 Nanospheres. *Chem. Eng. J.* **2022**, 430, 132738.
- (16) Bayliss, P.; Nowacki, W. Refinement of the Crystal Structure of Stibnite, Sb_2S_3 . *Z. Kristallogr.* **1972**, 135, 308–315.
- (17) McKee, D. O.; McMullan, J. T. Comment on the Structure of Antimony Trisulfide. *Z. Kristallogr.* **1975**, 142, 447–449.
- (18) Swinnea, J. S.; Tenorio, A. J.; Steinfink, H. $\text{Sb}_{10}\text{S}_{15}$, a Pb-free Analogue of Fülöppite, $\text{Pb}_3\text{Sb}_8\text{S}_{15}$. *Am. Mineral.* **1985**, 70, 1056–1058.
- (19) Lundegaard, L. F.; Miletich, R.; Balic-Zunic, T.; Makovicky, E. Equation of State and Crystal Structure of Sb_2S_3 between 0 and 10 GPa. *Phys. Chem. Minerals* **2003**, 30, 463–468.

- (20) Ibáñez, J.; Sans, J. A.; Popescu, C.; López-Vidrier, J.; Elvira-Betanzos, J. J.; Cuenca-Gotor, V. P.; Gomis, O.; Manjón, F. J.; Rodríguez-Hernández, P.; Muñoz, A. Structural, Vibrational, and Electronic Study of Sb₂S₃ at High Pressure. *J. Phys. Chem. C* **2016**, *120*, 10547–10558.
- (21) Efthimiopoulos, I.; Buchan, C.; Wang, Y. Structural Properties of Sb₂S₃ under Pressure: Evidence of an Electronic Topological Transition. *Sci. Reports* **2016**, *6*, 24246.
- (22) Dai, L.; Liu, K.; Li, H.; Wu, L.; Hu, H.; Zhuang, Y.; Yang, L.; Pu, C.; Liu, P. Pressure-Induced Irreversible Metallization Accompanying the Phase Transitions in Sb₂S₃. *Phys. Rev. B* **2018**, *97*, 024103.
- (23) Wang, Y.; Ma, Y.; Liu, G.; Wang, J.; Li, Y.; Li, Q.; Zhang, J.; Ma, Y.; Zou, G. Experimental Observation of the High Pressure Induced Substitutional Solid Solution and Phase Transformation in Sb₂S₃. *Sci. Reports* **2018**, *8*, 14795.
- (24) Cui, Z.; Bu, K.; Zhuang, Y.; Donnelly, M.-E.; Zhang, D.; Dalladay-Simpson, P.; Howie, R. T.; Zhang, J.; Lü, X.; Hu, Q. Phase Transition Mechanism and Bandgap Engineering of Sb₂S₃ at Gigapascal Pressures. *Commun. Chem.* **2021**, *4*, 125.
- (25) Ali, M. M. E.; Kong, P.; Ni, Y.; Wang, H.; Chen, Y. High Pressure Induced Decomposition of Antimony Trisulfide. *Mater. Today Commun.* **2021**, *29*, 102828.
- (26) Hu, C.; Xu, Y.; Gong, Y.; Yang, D.; Li, X.; Li, Y. Pressure-Induced Phase Transitions, Amorphization and Alloying in Sb₂S₃. *Phys. Chem. Chem. Phys.* **2022**, *24*, 10053–10061.
- (27) Červinka, L.; Hrubý, A. Structure of Amorphous and Glassy Sb₂S₃ and its Connection with the Structure of As₂X₃ Arsenic – Chalcogenide Glasses. *J. Non-Cryst. Solids* **1982**, *48*, 231–264.
- (28) Dalba, G.; Fornasini, P.; Giunta, G. Short Range Order of Amorphous Sb₂S₃ Thin Films: An X-ray Diffraction Study. *Solid State Commun.* **1987**, *62*, 773–776.
- (29) Dalba, G.; Fornasini, P.; Giunta, G.; Burattini, E. XRD and EXAFS Study of the Local Structure in Some Non-Crystalline Sb-S Compounds. *J. Non-Cryst. Solids* **1989**, *107*, 261–270.
- (30) Wuttig, M.; Yamada, N. Phase-Change Materials for Rewriteable Data Storage. *Nat. Mater.* **2007**, *6*, 824–832.
- (31) Raoux, S.; Wełnic, W.; Ielmini, D. Phase Change Materials and Their Application to Nonvolatile Memories. *Chem. Rev.* **2010**, *110*, 240–267.
- (32) Zhang, W.; Mazzarello, R.; Wuttig, M.; Ma, E. Designing Crystallization in Phase-Change Materials for Universal Memory and Neuro-Inspired Computing. *Nat. Rev. Mater.* **2019**, *4*, 150–168.
- (33) Kooi, B. J.; Wuttig, M. Chalcogenides by Design: Functionality through Metavalent Bonding and Confinement. *Adv. Mater.* **2020**, *32*, 1908302.
- (34) Akola, J.; Jones, R. O.; Kohara, S.; Kimura, S.; Kobayashi, K.; Takata, M.; Matsunaga, T.; Kojima, R.; Yamada, N. Experimentally Constrained Density-Functional Calculations of the Amorphous Structure of the Prototypical Phase-Change Material Ge₂Sb₂Te₅. *Phys. Rev. B* **2009**, *80*, 020201.
- (35) S. Caravati, M. Bernasconi and M. Parrinello, First-principles study of liquid and amorphous Sb₂Te₃, *Phys. Rev. B* **2010**, *81*, 014201.
- (36) Kolobov, A. V.; Tominaga, J. *Chalcogenides: Metastability and Phase Change Phenomena*; Springer: Berlin, 2012; pp 183–208.
- (37) Ahmed, S.; Wang, X.; Li, H.; Zhou, Y.; Chen, Y.; Sun, L.; Zhang, W.; Mazzarello, R. Change in Structure of Amorphous Sb–Te Phase-Change Materials as a Function of Stoichiometry. *Phys. Status Solidi RRL* **2021**, 2100064.
- (38) Hammersley, A. P.; Svensson, S. O.; Hanfland, M.; Fitch, A. N.; Häusermann, D. Two-Dimensional Detector Software: From Real Detector to Idealised Image or Two-Theta Scan. *High Pressure Res.* **1996**, *14*, 235–248.
- (39) Skinner, L. B.; Benmore, C. J.; Parise, J. B. Area Detector Corrections for High Quality Synchrotron X-ray Structure Factor Measurements. *Nucl. Instrum. Methods Phys. Res.* **2012**, *662*, 61–70.
- (40) Ohara, K.; Onodera, Y.; Kohara, S.; Koyama, C.; Masuno, A.; Mizuno, A.; Okada, J. T.; Tahara, S.; Watanabe, Y.; Oda, H.; Nakata, Y.; Tamaru, H.; Ishikawa, T.; Sakata, O. Accurate Synchrotron Hard X-ray Diffraction Measurements on High-Temperature Liquid Oxides. *Intern. J. Microgravity Sci. Appl.* **2020**, *37*, 370202.

- (41) Kohara, S.; Itou, M.; Suzuya, K.; Inamura, Y.; Sakurai, Y.; Ohishi, Y.; Takata, M. Structural Studies of Disordered Materials using High-Energy X-ray Diffraction from Ambient to Extreme Conditions. *J. Phys. Condens. Matter* **2007**, *19*, 506101.
- (42) Usuki, T.; Bokova, M.; Kassem, M.; Ohara, K.; Hannon, A. C.; Bychkov, E. Dimeric Molecular Structure of Molten Gallium Trichloride and a Hidden Evolution toward a Possible Liquid–Liquid Transition. *J. Phys. Chem. B* **2019**, *123*, 10260–10266.
- (43) Tverjanovich, A.; Khomenko, M.; Bereznev, S.; Fontanari, D.; Sokolov, A.; Usuki, T.; Ohara, K.; Le Coq, D.; Masselin, P.; Bychkov, E. Glassy GaS: Transparent and Unusually Rigid Thin Films for Visible to Mid-IR Memory Applications. *Phys. Chem. Chem. Phys.* **2020**, *22*, 25560–25573.
- (44) Frisch, M. J.; Trucks, G. W.; Schlegel, H. B.; Scuseria, G. E.; Robb, M. A.; Cheeseman, J. R.; Scalmani, G.; Barone, V.; Petersson, G. A.; Nakatsuji, H.; Li, X.; Caricato, M.; Marenich, A. V.; Bloino, J.; Janesko, B. G.; Gomperts, R.; Mennucci, B.; Hratchian, H. P.; Ortiz, J. V.; Izmaylov, A. F.; Sonnenberg, J. L.; Williams-Young, D.; Ding, F.; Lipparini, F.; Egidi, F.; Goings, J.; Peng, B.; Petrone, A.; Henderson, T.; Ranasinghe, D.; Zakrzewski, V. G.; Gao, J.; Rega, N.; Zheng, G.; Liang, W.; Hada, M.; Ehara, M.; Toyota, K.; Fukuda, R.; Hasegawa, J.; Ishida, M.; Nakajima, T.; Honda, Y.; Kitao, O.; Nakai, H.; Vreven, T.; Throssell, K.; Montgomery, J. A.; Peralta, J. E.; Ogliaro, F.; Bearpark, M. J.; Heyd, J. J.; Brothers, E. N.; Kudin, K. N.; Staroverov, V. N.; Keith, T. A.; Kobayashi, R.; Normand, J.; Raghavachari, K.; Rendell, A. P.; Burant, J. C.; Iyengar, S. S.; Tomasi, J.; Cossi, M.; Millam, J. M.; Klene, M.; Adamo, C.; Cammi, R.; Ochterski, J. W.; Martin, R. L.; Morokuma, K.; Farkas, O.; Foresman, J. B.; Fox, D. J. *Gaussian 16*, revision B.01; Gaussian, Inc.: Wallingford, CT, 2016.
- (45) Becke, A. D. Density-Functional Thermochemistry. III. The Role of Exact Exchange. *J. Chem. Phys.* **1993**, *98*, 5648–5653.
- (46) Lee, C.; Yang, W.; Parr, R. G. Development of the Colle-Salvetti Correlation-Energy Formula into a Functional of the Electron Density. *Phys. Rev. B* **1988**, *37*, 785.
- (47) Feller, D. The Role of Databases in Support of Computational Chemistry Calculations. *J. Comput. Chem.* **1996**, *17*, 1571–1586.
- (48) Peterson, K. A.; Figgen, D.; Goll, E.; Stoll, H.; Dolg, M. Systematically Convergent Basis Sets with Relativistic Pseudopotentials. II. Small-Core Pseudopotentials and Correlation Consistent Basis Sets for the Post-d Group 16–18 Elements. *J. Chem. Phys.* **2003**, *119*, 11113–11123.
- (49) Bacskey, G. B. A Quadratically Convergent Hartree-Fock (QCSCF) Method. Application to Closed Shell Systems. *Chem. Phys.* **1981**, *61*, 385–404.
- (50) Masselin, P.; Le Coq, D.; Cuisset, A.; Bychkov, E. Spatially Resolved Raman Analysis of Laser Induced Refractive Index Variation in Chalcogenide Glass. *Opt. Mater. Express* **2012**, *2*, 1768–1775.
- (51) Tverjanovich, A.; Cuisset, A.; Fontanari, D.; Bychkov, E. Structure of Se-Te Glasses by Raman Spectroscopy and DFT Modelling. *J. Am. Ceram. Soc.* **2018**, *101*, 5188–5197.
- (52) Kassem, M.; Bokova, M.; Tverjanovich, A. S.; Fontanari, D.; Le Coq, D.; Sokolov, A.; Masselin, P.; Kohara, S.; Usuki, T.; Hannon, A. C.; Benmore, C. J.; Bychkov, E. Bent HgI₂ Molecules in the Melt and Sulfide Glasses: Implications for Nonlinear Optics. *Chem. Mater.* **2019**, *31*, 4103–4112.
- (53) Kühne, T. D.; Iannuzzi, M.; Del Ben, M.; Rybkin, V. V.; Seewald, P.; Stein, F.; Laino, T.; Khaliullin, R. Z.; Schütt, O.; Schiffmann, F.; Golze, D.; Wilhelm, J.; Chulkov, S.; Bani-Hashemian, M. H.; Weber, V.; Borštnik, U.; Taillefumier, M.; Jakobovits, A. S.; Lazzaro, A.; Pabst, H.; Müller, T.; Schade, R.; Guidon, M.; Andermatt, S.; Holmberg, N.; Schenter, G. K.; Hehn, A.; Bussy, A.; Belleflamme, F.; Tabacchi, G.; Glöck, A.; Lass, M.; Bethune, I.; Mundy, C. J.; Plessl, C.; Watkins, M.; VandeVondele, J.; Krack, M.; Hutter, J. CP2K: An Electronic Structure and Molecular Dynamics Software Package – Quickstep: Efficient and Accurate Electronic Structure Calculations. *J. Chem. Phys.* **2020**, *152*, 194103.
- (54) Perdew, J. P.; Ernzerhof, M.; Burke, K. Rationale for Mixing Exact Exchange with Density Functional Approximations. *J. Chem. Phys.* **1996**, *105*, 9982–9985.
- (55) Adamo, C.; Barone, V. Toward Reliable Density Functional Methods without Adjustable Parameters: The PBE0 Model. *J. Chem. Phys.* **1999**, *110*, 6158–6170.

- (56) Tverjanovich, A.; Khomenko, M.; Benmore, C. J.; Bokova, M.; Sokolov, A.; Fontanari, D.; Kassem, M.; Usuki, T.; Bychkov, E. Bulk Glassy GeTe₂: A Missing Member of the Tetrahedral GeX₂ Family and a Precursor for the Next Generation of Phase-Change Materials. *Chem. Mater.* **2021**, *33*, 1031–1045.
- (57) Bokova, M.; Tverjanovich, A.; Benmore, C. J.; Fontanari, D.; Sokolov, A.; Khomenko, M.; Kassem, M.; Ozheredov, I.; Bychkov, E. Unraveling the Atomic Structure of Bulk Binary Ga–Te Glasses with Surprising Nanotectonic Features for Phase-Change Memory Applications. *ACS Appl. Mater. Interfaces* **2021**, *13*, 37363–37379.
- (58) Tverjanovich, A.; Khomenko, M.; Benmore, C. J.; Bereznev, S.; Sokolov, A.; Fontanari, D.; Kiselev, A.; Lotin, A.; Bychkov, E. Atypical Phase-Change Alloy Ga₂Te₃: Atomic Structure, Incipient Nanotectonic Nuclei, and Multilevel Writing. *J. Mater. Chem. C* **2021**, *9*, 17019–17032.
- (59) Kassem, M.; Bounazef, T.; Sokolov, A.; Bokova, M.; Fontanari, D.; Hannon, A. C.; Alekseev, I.; Bychkov, E. Deciphering Fast Ion Transport in Glasses: A Case Study of Sodium and Silver Vitreous Sulfides. *Inorg. Chem.* **2022**, *61*, 12870–12885.
- (60) Grimme, S.; Ehrlich, S.; Goerigk, L. Effect of the Damping Function in Dispersion Corrected Density Functional Theory. *J. Comput. Chem.* **2011**, *32*, 1456–1465.
- (61) Micoulaut, M. Communication: Van der Waals Corrections for an Improved Structural Description of Telluride Based Materials. *J. Chem. Phys.* **2013**, *138*, 061103.
- (62) Bouzid, A.; Massobrio, C.; Boero, M.; Ori, G.; Sykina, K.; Furet, E. Role of the van der Waals Interactions and Impact of the Exchange-Correlation Functional in Determining the Structure of Glassy GeTe₄. *Phys. Rev. B* **2015**, *92*, 134208.
- (63) Matsunaga, T.; Akola, J.; Kohara, S.; Honma, T.; Kobayashi, K.; Ikenaga, E.; Jones, R. O.; Yamada, N.; Takata, M.; Kojima, R. From Local Structure to Nanosecond Recrystallization Dynamics in AgInSbTe Phase-Change Materials. *Nat. Mater.* **2011**, *10*, 129–134.
- (64) Gereben, O.; Pusztai, L. RMC_POT, a Computer Code for Reverse Monte Carlo Modeling the Structure of Disordered Systems Containing Molecules of Arbitrary Complexity. *J. Comput. Chem.* **2012**, *33*, 2285–2291.
- (65) Hartwigsen, C.; Goedecker, S.; Hutter, J. Relativistic Separable Dual-Space Gaussian Pseudopotentials from H to Rn. *Phys. Rev. B* **1998**, *58*, 3641.
- (66) Nosé, S. A Molecular Dynamics Method for Simulations in the Canonical Ensemble. *Mol. Phys.* **1984**, *52*, 255–268.
- (67) Hoover, W. G. Canonical Dynamics: Equilibrium Phase-Space Distributions. *Phys. Rev. A* **1985**, *31*, 1695.
- (68) Le Roux, S.; Jund, P. Ring Statistics Analysis of Topological Networks: New Approach and Application to Amorphous GeS₂ and SiO₂ Systems. *Comput. Mater. Sci.* **2010**, *49*, 70–83.
- (69) Kohara, S.; Ohno, H.; Takata, M.; Usuki, T.; Morita, H.; Suzuya, K.; Akola, J.; Pusztai, L. Lead Silicate Glasses: Binary Network-Former Glasses with Large Amounts of Free Volume. *Phys. Rev. B* **2010**, *82*, 134209.
- (70) Heimbach, I.; Rhiem, F.; Beule, F.; Knodt, D.; Heinen, J.; Jones, R. O. pyMolDyn: Identification, Structure, and Properties of Cavities/Vacancies in Condensed Matter and Molecules. *J. Comput. Chem.* **2017**, *38*, 389–394.
- (71) Kawamoto, Y.; Tsuchihashi, S. The Properties and Structure of Glasses in the System As₂S₃–Sb₂S₃. *Yogyo-Kyokai-Shi* **1969**, *77*, 12–19.
- (72) N'Dri, K.; Sei, J.; Houphouet-Boigny, D.; Kra, G.; Jumas, J.-C. Estimation of Glass-Forming Ability and Glass Stability of Sb₂S₃–As₂S₃–Sb₂Te₃ Glasses by Thermal Properties. *J. Appl. Sci.* **2007**, *7*, 3167–3176.
- (73) N'Dri, K.; Houphouet-Boigny, D.; Jumas, J.-C.; Olivier-Fourcade, J. Electronegativity Difference, Atomic Size Parameter and Widths of Supercooled Liquid Regions of Sb₂S₃–As₂S₃–Sb₂Te₃ glasses. *J. Non-Cryst. Solids* **2011**, *357*, 145–149.
- (74) Janz, G. J.; Dampier, F. W.; Lakshminarayanan, G. R.; Lorenz, P. K.; Tomkins, R. P. T. *Molten Salts: Volume 1, Electrical Conductance, Density, and Viscosity Data*; National Standard Reference Data Series; NBS 15: Washington D.C., 1968; p. 98.

- (75) Mott, N. F.; Davis, E. A. *Electronic Processes in Non-Crystalline Materials*, 2nd ed.; Clarendon Press: Oxford, 1979; pp 28–37, 194–197, 491–497.
- (76) Guo, L.; Zhang, B.; Li, S.; Zhang, Q.; Buettner, M.; Li, L.; Qian, X.; Yan, F. Scalable and Efficient Sb₂S₃ Thin-Film Solar Cells Fabricated by Close Space Sublimation. *APL Mater.* **2019**, *7*, 041105.
- (77) Chen, J.; Qi, J.; Liu, R.; Zhu, X.; Wan, Z.; Zhao, Q.; Tao, S.; Dong, C.; Ashebir, G. Y.; Chen, W.; Peng, R.; Zhang, F.; Yang, S.; Tian, X.; Wang, M. Preferentially Oriented Large Antimony Trisulfide Single-Crystalline Cuboids Grown on Polycrystalline Titania Film for Solar Cells. *Commun. Chem.* **2019**, *2*, 121.
- (78) Guo, C.; Chen, J.; Li, G.; Liang, X.; Lai, W.; Yang, L.; Mai, Y.; Li, Z. Enhanced Electrical Conductivity of Sb₂S₃ Thin Film via C₆₀ Modification and Improvement in Solar Cell Efficiency. *Global Challenges* **2019**, 1800108.
- (79) Lojpur, V.; Joschko, M.; Graf, C.; Radmilović, N.; Novaković, M.; Validžić, I. Structural, Morphological, Optical, and Electronic properties of Amorphous Non-Doped and I and Sn Doped Sb₂S₃ Nanoparticles. *Mater. Sci. Semicond. Processing* **2022**, *137*, 106196.
- (80) Batsanov, S. S. Van der Waals Radii of Elements. *Inorg. Mater.* **2001**, *37*, 871–885.
- (81) Liu, Y.; Chua, K. T. E.; Sum, T. C.; Gan, C. K. First-Principles Study of the Lattice Dynamics of Sb₂S₃. *Phys. Chem. Chem. Phys.* **2014**, *16*, 345–350.
- (82) Lannin, J. S. Raman Scattering Properties of Amorphous As and Sb. *Phys. Rev. B* **1977**, *15*, 3863–3871.
- (83) Cheng, Z.; Milne, T.; Salter, P.; Kim, J. S.; Humphrey, S.; Booth, M.; Bhaskaran, H. Antimony Thin Films Demonstrate Programmable Optical Nonlinearity. *Sci. Adv.* **2021**, *7*, eabd7097.
- (84) Perales, F.; Lifante, G.; Agulló-Rueda, F.; de las Heras, C. Optical and Structural properties in the Amorphous to Polycrystalline Transition in Sb₂S₃ Thin Films. *J. Phys. D: Appl. Phys.* **2007**, *40*, 2440–2444.
- (85) Makreski, P.; Petruševski, G.; Ugarković, S.; Jovanovskic, G. Laser-Induced Transformation of Stibnite (Sb₂S₃) and Other Structurally Related Salts. *Vib. Spectrosc.* **2013**, *68*, 177–182.
- (86) Parize, R.; Cossuet, T.; Chaix-Pluchery, O.; Roussel, H.; Appert, E.; Consonni, V. In Situ Analysis of the Crystallization Process of Sb₂S₃ Thin Films by Raman Scattering and X-ray Diffraction. *Mater. Design* **2017**, *121*, 1–10.
- (87) Wang, J.; Qiao, Y.; Wang, T.; Yu, H.; Feng, Y.; Li, L. Two-Dimensional (2D) Amorphous Antimony (III) Trisulfide Nanosheets: Synthesis, Photoelectronic Property and their Transformation to Crystalline 1D Micro/Nanorods. *Inorg. Chem. Comm.* **2018**, *92*, 110–114.
- (88) Watanabe, I.; Noguchi, S.; Shimizu, T. Study on Local Structure in Amorphous Sb-S Films by Raman Scattering. *J. Non-Cryst. Solids* **1983**, *58*, 35–40.
- (89) Gutiérrez, Y.; Fernández-Pérez, A.; Rosales, S. A.; Cobianu, C.; Gheorghe, M.; Modreanu, M.; Saiz, J. M.; Moreno, F.; Losurdo, M. Polarimetry Analysis and Optical Contrast of Sb₂S₃ Phase Change Material. *Opt. Mater. Express* **2022**, *12*, 1531–1541.
- (90) Holubová, J.; Liška, M.; Chromčíková, M.; Černošková, E.; Černošek, Z. Structure of As₂S₃-Sb₂S₃ Glasses by Combined Raman Spectroscopy and a Thermodynamic Modelling Approach. *Phys. Chem. Glasses* **2012**, *53*, 31–36.
- (91) Pethes, I.; Nazabal, V.; Arib, J.; Kaban, I.; Darpentigny, J.; Welter, E.; Gutowski, O.; Bureau, B.; Messaddeq, Y.; Jónvári, P. Atomic Level Structure of Ge-Sb-S Glasses: Chemical Short Range Order and Long Sb-S Bonds. *J. Alloys Compd.* **2019**, *774*, 1009–1016.
- (92) Guan, S.; Sun, S.; Chen, D.; Zhang, J.; Kang, S.; Xu, T.; Lin, C. Formation and Physical and Structural Properties of Sb₂S₃-PbI₂ Chalcogenide Glasses. *J. Non-Cryst. Solids* **2021**, *570*, 120993.
- (93) Krebs, H.; Steffen, R. Neubestimmung der Nahordnung im Glasigen Selen, im Explosiven Antimon und im β- und γ-Arsen. *Z. Anorg. Allg. Chem.* **1964**, *327*, 224–237.
- (94) Winter, R.; Pilgrim, W.-C.; Egelstaff, P. A.; Chieux, P.; Anlauf, S.; Hensel, F. Neutron Scattering Study on Amorphous Sulphur. *Europhys. Lett.* **1990**, *11*, 225–228.
- (95) Bychkov, E.; Benmore, C. J.; Price, D. L. Compositional Changes of the First Sharp Diffraction Peak in Binary Selenide Glasses. *Phys. Rev. B* **2005**, *72*, 172107.

- (96) Bychkov, A.; Cuello, G. J.; Kohara, S.; Benmore, C. J.; Price, D. L.; Bychkov, E. Unraveling the Atomic Structure of Ge-Rich Sulfide Glasses. *Phys. Chem. Chem. Phys.* **2013**, *15*, 8487–8494.
- (97) Moss, S. C.; Price, D. L. Random Packing of Structural Units and the First Sharp Diffraction Peak in Glasses. In *Physics of Disordered Materials*; Adler, D., Fritzsche, H., Ovshinsky, S., Eds.; Plenum: New York, 1985; pp 77–95.
- (98) Barrett, C. S.; Cucka, P.; Haffner, K. The Crystal Structure of Antimony at 4.2, 78 and 298 °K. *Acta Cryst.* **1963**, *16*, 451–453.
- (99) Simdyankin, S. I.; Elliott, S. R.; Hajnal, Z.; Niehaus, T. A.; Frauenheim, Th. Simulation of Physical Properties of the Chalcogenide Glass As₂S₃ using a Density-Functional-Based Tight-Binding Method. *Phys. Rev. B* **2004**, *69*, 144202.
- (100) Mullen, D. J. E.; Nowacki, W. Refinement of the Crystal Structures of Realgar, AsS and Orpiment, As₂S₃. *Z. Kristallogr.* **1972**, *136*, 48–65.
- (101) Kampf, A. R.; Downs, R. T.; Housley, R. M.; Jenkins, R. A.; Hyrsl, J. Anorpiment, As₂S₃, the Triclinic Dimorph of Orpiment. *Mineralog. Mag.* **2011**, *75*, 2857–2867.
- (102) Bychkov, E.; Wortmann, G. ¹²¹Sb-Mössbauer Study of Insulating and Ion-Conducting Antimony Chalcogenide-Based Glasses. *J. Non-Cryst. Solids* **1993**, *159*, 162–172.
- (103) Ruby, S. L.; Kalvius, G. M.; Beard, G. B.; Snyder, R. E. Interpretation of Mössbauer Measurements in Tin and Antimony. *Phys. Rev.* **1967**, *159*, 239–245.
- (104) Caravati, S.; Bernasconi, M.; Parrinello, M. First-Principles Study of Liquid and Amorphous Sb₂Te₃. *Phys. Rev. B* **2010**, *81*, 014201.
- (105) Akola, J.; Jónvári, P.; Kaban, I.; Voleská, I.; Kolář, J.; Wágner, T.; Jones, R. O. Structure, Electronic, and Vibrational Properties of Amorphous AsS₂ and AgAsS₂: Experimentally Constrained Density Functional Study. *Phys. Rev. B* **2014**, *89*, 064202.
- (106) Wang, X.; Li, Z.; Kavanagh, S. R.; Ganose, A. M.; Walsh, A. Lone Pair Driven Anisotropy in Antimony Chalcogenide Semiconductors. *Phys. Chem. Chem. Phys.* **2022**, *24*, 7195–7202.
- (107) Grigas, J.; Talik, E.; Lazauskas, V. X-ray Photoelectron Spectroscopy of Sb₂S₃ Crystals. *Phase Transitions* **2002**, *75*, 323–337.
- (108) Ben Nasr, T.; Maghraoui-Meherzi, H.; Ben Abdallah, H.; Bennaceur, R. Electronic Structure and Optical Properties of Sb₂S₃ crystal. *Physica B* **2011**, *406*, 287–292.
- (109) Xu, M.; Gu, R.; Qiao, C.; Tong, H.; Cheng, X.; Wang, C.-Z.; Ho, K.-M.; Wang, S.; Miao, X.; Xu, M. Unraveling the Structural and Bonding Nature of Antimony Sesquichalcogenide Glass for Electronic and Photonic Applications. *J. Mater. Chem. C* **2021**, *9*, 8057–8065.
- (110) Gutiérrez, Y.; Ovvyan, A. P.; Santos, G.; Juan, D.; Rosales, S. A.; Junquera, J.; García-Fernández, P.; Dicorato, S.; Giangregorio, M. M.; Dilonardo, E.; Palumbo, P.; Modreanu, M.; Resl, J.; Ishchenko, O.; Garry, G.; Jonuzi, T.; Georghe, M.; Cobianu, C.; Hingerl, K.; Cobet, C.; Moreno, F.; Pernice, W. H. P.; Losurdo, M. Interlaboratory Study on Sb₂S₃ Interplay between Structure, Dielectric Function, and Amorphous-to-Crystalline Phase Change for Photonics. *iScience* **2022**, *25*, 104377.
- (111) Kalikka, J.; Akola, J.; Jones, R.O.; Kohara, S.; Usuki, T. Amorphous Ge₁₅Te₈₅: density functional, high-energy X-ray and neutron diffraction study. *J. Phys.: Condens. Matter.* **2012**, *24*, 015802.
- (112) Orava, J.; Hewak, D. W.; Greer, A. L. Fragile-to-Strong Crossover in Supercooled Liquid Ag-In-Sb-Te Studied by Ultrafast Calorimetry. *Adv. Funct. Mater.* **2015**, *25*, 4851–4858.
- (113) Wei, S.; Lucas, P.; Angell, C. A. Phase Change Alloy Viscosities down to T_g using Adam-Gibbs-Equation Fittings to Excess Entropy Data: A Fragile-to-Strong Transition. *J. Appl. Phys.* **2015**, *118*, 034903.
- (114) Wei, S.; Lucas, P.; Angell, C. A. Phase-Change Materials: The View from the Liquid Phase and the Metallicity Parameter. *MRC Bull.* **2019**, *44*, 691–698.
- (115) Pries, J.; Weber, H.; Benke-Jacob, J.; Kaban, I.; Wei, S.; Wuttig, M.; Lucas, P. Fragile-to-Strong Transition in Phase-Change Material Ge₃Sb₆Te₅. *Adv. Func. Mater.* **2022**, 2202714.
- (116) Zhu, W.; Gulbiten, O.; Aitken, B.; Sen, S. Viscosity, Enthalpy Relaxation and Liquid-Liquid Transition of the Eutectic Liquid Ge₁₅Te₈₅. *J. Non-Cryst. Solids* **2021**, *554*, 120601.

- (117) Huang, R.; Chavez, I.; Taute, K. M.; Lukić, B.; Jeney, S.; Raizen, M. G.; Florin, E.-L. Direct Observation of the Full Transition from Ballistic to Diffusive Brownian Motion in a Liquid. *Nat. Phys.* **2011**, *7*, 576–580.
- (118) Chernov, A. P.; Dembovsky, S. A.; Makhova, V. M. Viscosity and Structure of Glasses in the $\text{As}_2\text{X}_3\text{--AsI}_3$ System. *Izv. Akad. Nauk SSSR, Neorg. Mater.* **1970**, *6*, 823–825.
- (119) Shchukina, N. E.; Orlova, G. M.; Chalabyan, G. A. The Viscosity and Elastic Properties of Glasses in the Arsenic–Sulfur–Thallium System. *Fiz. Khim. Stekla* **1979**, *5*, 223–228.
- (120) Nemilov, S. V. The Viscosity and Elastic Properties of Melts and Glasses in the As–S System and their Valence-Bond Structure. *Fiz. Khim. Stekla* **1979**, *5*, 398–409.
- (121) Chaussemy, G.; Fornazero, J.; Mackowski, J.-M. Relationship between Viscosity and Structure in $\text{As}_x\text{S}_{1-x}$ Molten Materials. *J. Non-Cryst. Solids* **1983**, *58*, 219–234.
- (122) Tverjanovich, A. S. Temperature Dependence of the Viscosity of Chalcogenide Glass-Forming Melts. *Glass Phys. Chem.* **2003**, *29*, 532–536.
- (123) Shánělová, J.; Košťál, P.; Málek, J. Viscosity of $(\text{GeS}_2)_x(\text{Sb}_2\text{S}_3)_{1-x}$ Supercooled Melts. *J. Non-Cryst. Solids* **2006**, *352*, 3952–3955.
- (124) Mauro, J. C.; Yue, Y.; Ellison, A. J.; Gupta, P. K.; Allan, D. C. Viscosity of Glass-Forming Liquids. *Proc. Natl. Acad. Sci. U.S.A.* **2009**, *106*, 19780–19784.
- (125) Košťál, P.; Shánělová, J.; Málek, J. Viscosity of Chalcogenide Glass-Formers. *Int. Mater. Rev.* **2019**, *65*, 63–101.
- (126) Yuan, B.; Aitken, B. G.; Sen, S. Viscoelastic Behavior and Fragility of Se-deficient Chalcogenide Liquids in As–P–Se System. *J. Non-Cryst. Solids* **2022**, *16*, 100128.
- (127) Kassem, M.; Benmore, C. J.; Usuki, T.; Ohara, K.; Tverjanovich, A.; Bokova, M.; Brazhkin, V. V.; Bychkov, E. Transient Mesoscopic Immiscibility, Viscosity Anomaly and High Internal Pressure at the Semiconductor–Metal Transition in Liquid Ga_2Te_3 . *J. Phys. Chem. Lett.* **2022**, *13*, 10843–10850.
- (128) Rödl, T.; Weihrich, R.; Wack, J.; Senker, J.; Pfitzner, A. Rational Syntheses and Structural Characterization of Sulfur-Rich Phosphorus Polysulfides: $\alpha\text{-P}_2\text{S}_7$ and $\beta\text{-P}_2\text{S}_7$. *Angew. Chem. Int. Ed.* **2011**, *50*, 10996–11000.
- (129) Koudelka, L.; Pisárčik, M.; Gutenov, M. S.; Blinov, L. N. Raman Spectra and Short-Range Order in P_xS_{1-x} Glasses. *J. Mater. Sci. Lett.* **1989**, *8*, 933–934.
- (130) Tullius, M.; Lathrop, D. A.; Eckert, H. Glasses in the System Phosphorus–Sulfur: A ^{31}P Spin-Echo and High-speed MAS-NMR Study of Atomic Distribution and Local Order. *J. Phys. Chem.* **1990**, *94*, 2145–2150.
- (131) Lyda, C. M.; Leone, J. M.; Bankert, M. A.; Xia, Y.; Eckert, H. Structural Studies of Phosphorus–Sulfur–Tellurium Glasses by ^{31}P MAS NMR and Vibrational Spectroscopies. *Chem. Mater.* **1994**, *6*, 1934–1939.
- (132) Shibao, R. K.; Xia, Y.; Srdanov, V. I.; Eckert, H. Plasma-Enhanced Chemical Vapor Deposited Phosphorus Sulfide Films. Characterization by Raman and Solid-State NMR Spectroscopies and Comparison to Melt-Quenched Glassy Materials. *Chem. Mater.* **1995**, *7*, 1631–1638.
- (133) Novoselova, A.V.; Pashinkin, A.S. *Vapor Pressures of Volatile Metal Chalcogenides*; Nauka: Moscow, 1978; pp 78–83.
- (134) Lau, K. H.; Brittain, R. D.; Hildenbrand, D. L. Vaporization of As_2S_3 , and the Dissociation Energy of AsS . *J. Phys. Chem.* **1982**, *86*, 4429–4432.
- (135) Solin, S. A.; Papatheodorou, G. N. Irreversible Thermostructural Transformations in Amorphous As_2S_3 Films: A Light-Scattering Study. *Phys. Rev. B* **1977**, *15*, 2084–2090.
- (136) Nemanich, R. J.; Connell, G. A. N.; Hayes, T. M.; Street, R. A. Thermally Induced Effects in Evaporated Chalcogenide Films. I. Structure. *Phys. Rev. B* **1978**, *18*, 6900–6914.
- (137) Slade, M.L.; Zallen, R. Raman Spectra of As_4S_4 Polymorphs: Structural Implications for Amorphous As_2S_3 Films. *Solid State Commun.* **1979**, *30*, 357–360.
- (138) De Neufville, J. P.; Moss, S. C.; Ovshinsky, S. R. Photostructural Transformations in Amorphous As_2Se_3 and As_2S_3 Films. *J. Non-Cryst. Solids*, **1973**, *13*, 191–223.
- (139) Daniel, M. F.; Leadbetter, A. J.; Wright, A. C.; Sinclair, R. N. The Structure of Vapour-Deposited Arsenic Sulphides. *J. Non-Cryst. Solids* **1979**, *32*, 271–293.

- (140) Greenwood, N.N.; Earnshaw, A. *Chemistry of the Elements*, 2nd ed.; Butterworth-Heinemann: Oxford, 1997; pp 578–583.
- (141) Lukaszewicz, K.; Stepen-Damm, Yu.; Pietraszko, A.; Kajokas, A.; Grigas, J. Crystal Structure, Thermal Expansion, Dielectric Permittivity and Phase Transitions of Bi_2S_3 . *Polish J. Chem.* **1999**, *73*, 541–546.
- (142) Tanaka, K. Chemical and Medium-Range Orders in As_2S_3 Glass. *Phys. Rev. B* **1987**, *36*, 9746–9752.
- (143) Ito, T.; Morimoto, N.; Sadanaga, R. The Crystal Structure of Realgar. *Acta Crystallogr.* **1952**, *5*, 775–782.
- (144) Hosokawa, S.; Sakaguchi, Y.; Hiasa, H.; Tamura, K. Optical Absorption Spectra of Liquid As_2S_3 and As_2Se_3 over a Wide Temperature Range. *J. Phys.: Condens. Matter* **1991**, *3*, 6673–6677.
- (145) Alekseev, V. A.; Andreev, A. A.; Sadovskii, M. V. Semiconductor-Metal Transition in Liquid Semiconductors. *Sov. Phys. Usp.* **1980**, *23*, 551–575.
- (146) Liang, X.; Feng, Y.; Dang, W.; Huang, H.; Wang, X.; Guo, Y.; Shen, K.; Schropp, R. E. I.; Li, Z.; Mai, Y. High-Efficiency Flexible Sb_2Se_3 Solar Cells by Back Interface and Absorber Bulk Deep-Level Trap Engineering. *ACS Energy Lett.* **2023**, *8*, 213–221.
- (147) Linhart, W. M.; Zelewski, S. J.; Scharoch, P.; Dybała, F.; Kudrawiec, R. Nesting-Like Band Gap in Bismuth Sulfide Bi_2S_3 . *J. Mater. Chem. C* **2021**, *9*, 13733–13738.
- (148) Lan, M.; Wang, Y.; Dong, X.; Yang, F.; Zheng, N.; Wang, Y.; Ma, H.; Zhang, X. Controllable Fabrication of Sulfur-Vacancy-Rich Bi_2S_3 Nanorods with Efficient Near-Infrared Light Photocatalytic for Nitrogen Fixation. *Appl. Surf. Sci.* **2022**, *591*, 153205.
- (149) Park, J.-W.; Baek, S. H.; Kang, T. D.; Lee, H.; Kang, Y.-S.; Lee, T.-Y.; Suh, D.-S.; Kim, K. J.; Kim, C. K.; Khang, Y. H.; Da Silva, J. L. F.; Wei, S.-H. Optical Properties of $(\text{GeTe}, \text{Sb}_2\text{Te}_3)$ Pseudobinary Thin Films Studied with Spectroscopic Ellipsometry. *Appl. Phys. Lett.* **2008**, *93*, 021914.
- (150) Soignard, E.; Tsiok, O. B.; Tverjanovich, A. S.; Bychkov, A.; Sokolov, A.; Brazhkin, V. V.; Benmore, C. J.; Bychkov, E. Pressure-Driven Chemical Disorder in Glassy As_2S_3 up to 14.7 GPa, Post-densification Effects, and Applications in Materials Design. *J. Phys. Chem. B* **2020**, *124*, 430–442.
- (151) Ichikawa, T. Electron Diffraction Study of the Local Atomic Arrangement in Amorphous Tellurium Films. *Phys. Stat. Solidi B* **1973**, *56*, 707–715.
- (152) Suzuki, S.; Maruyama, K.; Misawa, M. Structural Analysis of Liquid Chalcogen by RMC Modeling with a Dimer Molecule Model. *J. Phys. Soc. Japan* **2000**, *69*, 3576–3580.
- (153) Akola, J.; Jones, R. O.; Kohara, S.; Usuki, T.; Bychkov, E. Density Variations in Liquid Tellurium: Roles of Rings, Chains, and Cavities. *Phys. Rev. B* **2010**, *81*, 094202.